JGR Earth Surface

RESEARCH ARTICLE
10.1029/2023JF007201

Modeling Cosmogenic Nuclides in Transiently Evolving Topography and Chemically Weathering Soils

Miles M. Reed[1], **Ken L. Ferrier**[1], **and J. Taylor Perron**[2]

[1]Department of Geoscience, University of Wisconsin-Madison, Madison, WI, USA, [2]Department of Earth, Atmospheric, and Planetary Sciences, Massachusetts Institute of Technology, Cambridge, MA, USA

Key Points:

- We developed a model to compute terrestrial cosmogenic nuclide (TCN) concentrations in transiently evolving topography and chemically weathering soils
- TCN-based denudation rates track actual denudation rates more closely during responses to changes in uplift rate than to changes in climate
- Soil chemical weathering influences modeled TCN concentrations, confirming that this should be accounted for in TCN-based denudation rates

Supporting Information:

Supporting Information may be found in the online version of this article.

Correspondence to:

M. M. Reed,
miles.reed@wisc.edu

Citation:

Reed, M. M., Ferrier, K. L., & Perron, J. T. (2023). Modeling cosmogenic nuclides in transiently evolving topography and chemically weathering soils. *Journal of Geophysical Research: Earth Surface*, *128*, e2023JF007201. https://doi.org/10.1029/2023JF007201

Received 12 APR 2023
Accepted 25 SEP 2023

Abstract Terrestrial cosmogenic nuclides (TCN) are widely employed to infer denudation rates in mountainous landscapes. The calculation of an inferred denudation rate (D_{inf}) from TCN concentrations is typically performed under the assumptions that denudation rates were steady during TCN accumulation and that soil chemical weathering negligibly impacted soil mineral abundances. In many landscapes, however, denudation rates were not steady and soil composition was significantly impacted by chemical weathering, which complicates interpretation of TCN concentrations. We present a landscape evolution model that computes transient changes in topography, soil thickness, soil mineralogy, and soil TCN concentrations. We used this model to investigate TCN responses in transient landscapes by imposing idealized perturbations in tectonically (rock uplift rate) and climatically sensitive parameters (soil production efficiency, hillslope transport efficiency, and mineral dissolution rate) on initially steady-state landscapes. These experiments revealed key insights about TCN responses in transient landscapes. (a) Accounting for soil chemical erosion is necessary to accurately calculate D_{inf}. (b) Responses of D_{inf} to tectonic perturbations differ from those to climatic perturbations, suggesting that spatial and temporal patterns in D_{inf} are signatures of perturbation type and magnitude. (c) If soil chemical erosion is accounted for, basin-averaged D_{inf} inferred from TCN in stream sediment closely tracks actual basin-averaged denudation rate, showing that D_{inf} is a reasonable proxy for actual denudation rate, even in many transient landscapes. (d) Response times of D_{inf} to perturbations increase with hillslope length, implying that response times should be sensitive to the climatic, biological, and lithologic processes that control hillslope length.

Plain Language Summary In geomorphology, the rate at which mountains wear down is commonly inferred from concentrations of cosmogenic nuclides in minerals in soil or river sand. Cosmogenic nuclides are isotopes that build up in minerals during exposure to high energy particles from space, accumulating at a rate that depends on the degree to which the soil is chemically altered and the mountain's erosion rate itself. To explore how cosmogenic nuclide concentrations change in soil over time, we developed a computer model that tracks cosmogenic nuclide concentrations in soil across a landscape. We used this model to perform two model experiments: one driven by a change in the rate at which the bedrock is rising (the so-called tectonic experiment), and the other driven by a change in rainfall (the climatic experiment). Our experiments confirm that accounting for soil composition is necessary to accurately infer erosion rate. They also show that cosmogenic nuclide concentrations respond differently to tectonic changes than climatic changes, implying that patterns of cosmogenic nuclide concentrations may reflect perturbation type. The time it takes cosmogenic nuclide concentrations to respond to a perturbation increases with the length of the hills from the ridge to the valley, implying that response times should be influenced by climate, life, and rock type. These results show how this model can be used to explore how mountainous topography, soils, and cosmogenic nuclides change simultaneously. Our model will be a useful tool for improving field measurements of cosmogenic nuclide concentrations in soil and in stream sediment.

1. Introduction

The denudation of mountainous landscapes is central to many Earth processes. It modifies topography (e.g., Gilbert, 1877), accelerates soil production (e.g., Heimsath et al., 1997), affects soil nutrient supply (e.g., Y. Lucas, 2001), focuses rock exhumation (e.g., Willett, 1999), perturbs sea level by unloading continental surfaces (e.g., Dalca et al., 2013; Ferrier et al., 2017), and modulates Earth's climate by affecting weathering rates of silicates and sulfides (e.g., Torres et al., 2014; Walker et al., 1981). Deciphering the controls on denudation rate is therefore of wide interest across the geosciences.

At present, the most common tool for measuring millennial-scale denudation rates is terrestrial cosmogenic nuclides (TCN). Concentrations of TCN in host minerals (e.g., ^{10}Be in quartz) can be used to infer denudation rates averaged over a catchment drainage area (Bierman & Steig, 1996; Brown et al., 1995; Granger et al., 1996) or at a point on a hillslope (Dixon & von Blanckenburg, 2012; Lal, 1991; Riebe et al., 2003). Over the past few decades, TCN-inferred estimates of denudation rate (which we refer to as D_{inf}) have been measured in thousands of places (Codilean et al., 2022) and have been harnessed to investigate many things, including the influence of climate and tectonics on denudation rate (e.g., Ferrier et al., 2012; Godard et al., 2020; Riebe et al., 2004; West et al., 2005). The standard equations used to invert TCN concentrations for D_{inf} assume steady state—that is, TCN-bearing minerals have been exhumed from depth to the surface at a steady rate and that the subsurface depth profile of TCN concentrations is invariant in time (Lal, 1991).

In landscapes that are out of steady state, TCN concentrations differ from what they would be in steady state. If conventional expressions for steady-state D_{inf} were applied to TCN concentrations in transient landscapes, then the resulting estimates of D_{inf} would differ from the actual denudation rates by an amount that depends on the magnitude of the landscape's deviation from steady state (e.g., Bierman & Steig, 1996; Mudd, 2017; von Blanckenburg, 2006). Ferrier and Kirchner (2008) observed that D_{inf} is robust to minor deviations from steady state, which suggests that D_{inf} is likely to be an accurate approximation of the true denudation rate in many landscapes. More practically, the Ferrier and Kirchner (2008) simulations imply that errors in D_{inf} associated with transience are smaller than our ignorance of what denudation rates actually were over the past few thousand years (an ignorance that is large in most landscapes, and in some landscapes is unbounded), given the absence of alternative methods for measuring millennial-scale denudation rates. This underscores the usefulness of measuring D_{inf} with TCN, despite uncertainties associated with transient conditions. Nonetheless, if deviations from steady state are not accounted for, they could lead to errors in D_{inf} of unknown size. It would be useful to be able to interpret those sources of error as accurately as possible.

Concerns about transients are common because transient landscapes are common. Stream capture (Beeson et al., 2017), exhumation of rocks of different strengths (Forte et al., 2016; Zondervan et al., 2020), climatic shifts (Marshall et al., 2017), and changes in tectonic movements (Hurst et al., 2019) can all give rise to transients in topography and soil composition (Ferrier & West, 2017). Moreover, detecting landscape transience can be difficult at the soil profile or hillslope scale (Heimsath et al., 2002; Hippe et al., 2021). Recent work with paired nuclides has presented a method for detecting the magnitude but not the timing of transient conditions (Skov et al., 2019), but quantifying the history of deviations from steady state remains challenging.

The recognition that landscapes are rarely in perfect steady state has inspired efforts to investigate transient effects on TCN through numerical models. Small et al. (1999) developed the first hillslope-profile model of TCN conservation that included process representations of hillslope sediment transport and soil production. Anderson (2015) extended the hillslope-profile framework to investigate the influence of soil mixing on particle transit times and TCN concentrations. Heimsath (2006) modeled the response of TCN depth profiles to changes in physical erosion rate and showed that TCN-inferred erosion rates lag behind actual rates. Mudd (2017) modeled TCN responses in a 2D landscape to changes in uplift rate, hillslope transport, and fluvial incision efficiency and showed that D_{inf} responses to climate-related parameters closely matched the forcing while D_{inf} responses to uplift rate were damped and lagged. These studies and many others have advanced our understanding of the effects of transients on TCN concentrations.

To date, no study has investigated the sensitivity of TCN to transient conditions in a full 2D landscape evolution model that includes explicit treatment of eroding and chemically weathering soil. That is our goal here. In this study, we present a model to compute TCN concentrations in soil and the underlying rock, and we show how to apply this model across landscapes undergoing simultaneous changes in topography, soil production rate, physical erosion rate, chemical erosion rate, soil thickness, and soil composition. This extends the model of Ferrier and Perron (2020), which accounted for production, transport, and chemical erosion of soils in transiently evolving topography but did not include TCN.

A key aspect of this model is that it is able to account for the effects of soil chemical erosion on TCN. These effects can be significant. Small et al. (1999) and Riebe et al. (2001) recognized that chemical weathering of soluble minerals increases the exposure times of dissolution-resistant host minerals such as quartz to cosmic rays, and hence increases TCN concentrations in quartz beyond what they would be in the absence of chemical weathering. If this additional exposure were neglected, this would yield erroneously low estimates of TCN-based denudation

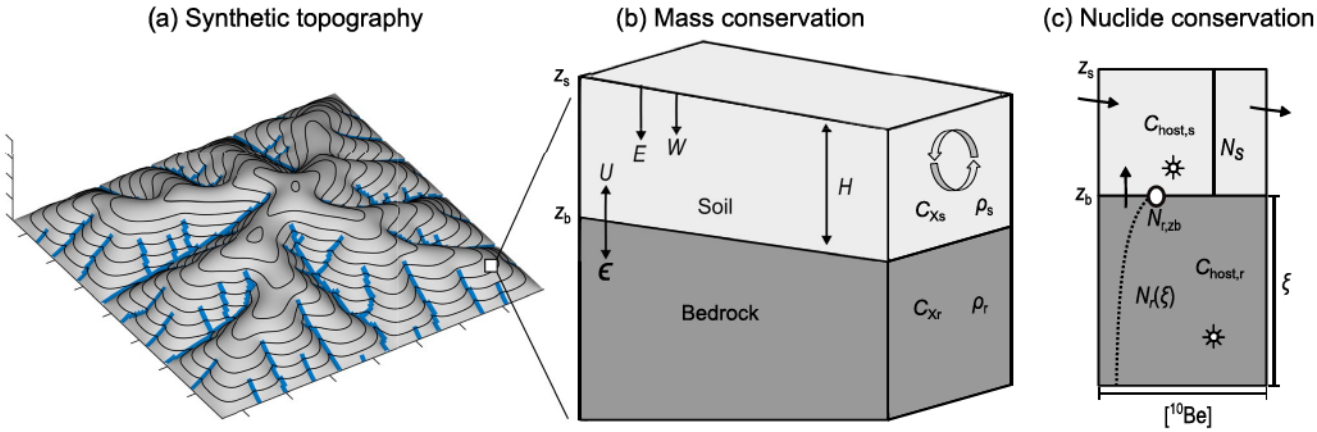

Figure 1. Schematic of model framework (Section 2.1). At each grid point within a synthetic landscape (panel a), soil mass (panel b) and cosmogenic nuclides (panel c) are conserved. (a) Stream channels indicated in blue, soil-mantled hillslopes in shaded relief with elevation contours. (b) Soil thickness (H) is governed by physical erosion rate (E), chemical erosion rate (W), and soil production rate (ϵ). Elevation of the bedrock-soil boundary (z_b) is governed by bedrock uplift rate (U) and ϵ. Soil mineral concentrations (C_{Xs}) are determined by mineral supply from ϵ and losses through E and W. Soil and bedrock densities (ρ_s and ρ_r) are held constant. (c) Soil terrestrial cosmogenic nuclides (TCN) concentrations (N_s) are determined by supply from bedrock, hillslope soil transport, and cosmogenic nuclide production and decay (star symbol). In the soil, N_s (^{10}Be in this case) is uniform with depth, consistent with a vertically well-mixed soil. The TCN concentration at soil-bedrock boundary ($N_{r,zb}$) arises through the calculation of a bedrock TCN profile N_r at a depth ξ below the soil-bedrock interface through time.

rate. Riebe and Granger (2013) extended this work to consider chemical erosion in deep saprolite, showing that D_{inf} can be in error by tens of percent if chemical erosion is neglected. Because our simulations calculate soil chemical depletion directly, they are able to confirm the importance of accounting for soil chemical erosion in TCN-based estimates of denudation rate. More generally, our simulations show how this model can be used to investigate the influence of tectonic and climatic perturbations on transiently evolving hillslopes and illustrate how to identify transient conditions from multiple TCN measurements across a landscape.

2. Methods

2.1. Model Description

We designed our model to capture simultaneous responses of TCN, topography, soil thickness, and soil composition to changes in boundary conditions (e.g., bedrock uplift rate) and rates of soil production, transport, and chemical weathering. The model does not treat bare-bedrock hillslopes, so application of this model is restricted to soil-mantled landscapes. We incorporated nonlinear hillslope soil transport and TCN conservation into the coupled landscape evolution-soil mineralogy model of Ferrier and Perron (2020). The model tracks and conserves TCN concentrations in the soil, at the soil-bedrock interface, and in deeper bedrock (Figure 1). Our aim was to construct and test a model that simulates cosmogenic nuclide production and transport in soil-mantled uplands, a common type of landscape.

In our model, stream channels are restricted to vertical movement relative to the hillslopes and set the local base-level of the hillslopes (Mudd & Furbish, 2007). We do have the capacity to specify a rate law for stream channel incision (Text S4 in Supporting Information S1), but, in this work, we wish to focus solely on the distributed hillslope response for simplicity. During transient conditions, rates of hillslope soil transport, soil production, and mineral dissolution vary across the landscape. This results in temporal and spatial variations in soil thickness, soil mineral concentrations, and TCN concentrations. In this section, we detail the governing equations, numerical implementation, and several methods for solving for inferred denudation rate using the modeled TCN concentrations.

2.2. Governing Equations for Topography, Soil Thickness, and Soil Composition

The elevation of the bedrock-soil boundary, z_b, increases at a bedrock uplift rate, U (L T^{-1}), and decreases at a soil production rate, ϵ (L T^{-1}). The change in z_b is expressed as

$$\frac{\partial z_b}{\partial t} = U - \epsilon_0 e^{-H/H_0}. \quad (1)$$

In Equation 1, the second term is the exponential soil production function (Heimsath et al., 1997, 1999), where H (L) is soil thickness, H_0 (L) is the characteristic length that regulates soil production rate with regard to H, and ϵ_0 (L T^{-1}) is the maximum soil production rate at zero H. U is imposed upon the landscape, and a static channel network incises at a rate equal to U. H changes via soil production rate, the divergence of downslope soil transport, and chemical erosion rate:

$$\frac{\partial H}{\partial t} = \frac{\rho_r}{\rho_s}\epsilon_0 e^{-H/H_0} - \nabla \cdot q_s - W, \quad (2)$$

where ρ_r and ρ_s are bedrock and soil density (M L^{-3}), respectively. In our model, ρ_r and ρ_s are time-invariant. The downslope volumetric flux of soil per unit contour width, q_s (L^2 T^{-1}), increases nonlinearly with respect to hillslope gradient of the model surface elevation, ($z_s = z_b + H$), and is defined as

$$q_s = \frac{-K_{nl}\nabla z_s}{1 - (|\nabla z_s|/S_c)^2}. \quad (3)$$

Here, K_{nl} is the soil transport coefficient (L^2 T^{-1}), ∇z_s is the local hillslope gradient, and S_c is the critical gradient (Roering et al., 1999, 2001). Our framework is flexible enough to adopt other formulations for q_s, such as those that depend on soil thickness (Braun et al., 2001). For simplicity, the simulations we show in this study are governed by Equation 3. This translates into a physical erosion rate E (L T^{-1}) by taking the divergence of q_s (Roering et al., 1999):

$$E = -K_{nl}\left[\frac{\nabla^2 z_s}{1 - (|\nabla z_s|/S_c)^2} + 2\frac{\left(\frac{\partial z_s}{\partial x}\right)^2\left(\frac{\partial^2 z_s}{\partial x^2}\right) + \left(\frac{\partial z_s}{\partial y}\right)^2\left(\frac{\partial^2 z_s}{\partial y^2}\right) + 2\left(\frac{\partial z_s}{\partial x}\frac{\partial z_s}{\partial y}\frac{\partial^2 z_s}{\partial x \partial y}\right)}{S_c^2\left(1 - (|\nabla z_s|/S_c)^2\right)^2}\right], \quad (4)$$

where x and y are the two axes of a regular grid. As implemented, E is limited by the thickness of the explicitly modeled soil layer, H, such that, for a given timestep, erosion can never be greater than H (Text S2 in Supporting Information S1). This parameterization for soil transport is most applicable to nonlinear creep and is not directly applicable to large discrete events such as deep-seated landslides. Chemical erosion rate, W (L T^{-1}), is calculated following Ferrier and Kirchner (2008) as the difference between mineral dissolution and secondary mineral formation rates summed over n mineral species throughout the soil:

$$W = H\sum_{j=1}^{n}\left(k_j A_j C_{js} - \frac{s_j w_j}{\rho_s}\right), \quad (5)$$

where k_j (mol L^{-2} T^{-1}), A_j (L^2 mol^{-1}), C_{js} (M M^{-1}), s_j (mol L^{-3} T^{-1}), and w_j (M mol^{-1}) are the mineral dissolution constant, specific surface area, soil mineral concentration, secondary mineral production rate, and molar mass of the jth mineral from the set of n soil minerals, respectively.

The concentration of an individual soil mineral X, C_{Xs} (M M^{-1}), evolves through the competition between dissolution and mineral supply. We assume a well-mixed soil such that mineral concentration is independent of soil depth (Ferrier & West, 2017). Soil production, hillslope soil transport, mineral dissolution, secondary mineral formation, and the mass losses of the other mineral phases combine to modify a mineral's concentration:

$$\frac{\partial C_{Xs}}{\partial t} = \frac{\rho_r}{\rho_s H}\epsilon_0 e^{-H/H_0}(C_{Xr} - C_{Xs}) - \frac{q_s}{H}\cdot\nabla C_{Xs} - k_X A_x C_{Xs} + \frac{s_X w_X}{\rho_s} + C_{Xs}\sum_{j=1}^{n}\left(k_j A_j C_{js} - \frac{s_j w_j}{\rho_s}\right). \quad (6)$$

Here, C_{Xr} (M M^{-1}) is the concentration of mineral X in the bedrock. This formulation differs from that in Ferrier and Perron (2020) only in the transport term (second term), where q_s is represented as a nonlinear function of hillslope gradient (Equation 3) rather than a linear function of it (Yoo et al., 2007). Combining Equations 1 and 2, the rate of change of z_s is expressed as

$$\frac{\partial z_s}{\partial t} = U - E + \left(\frac{\rho_r}{\rho_s} - 1\right)\epsilon_0 e^{-H/H_0} - H\sum_{j=1}^{n}\left(k_j A_j C_{js} - \frac{s_j w_j}{\rho_s}\right). \quad (7)$$

Model outputs can exhibit nonlinear behavior during transient conditions through the interacting changes in topography, mineral supply from soil production, soil thickness, and chemical erosion (Ferrier & Perron, 2020).

2.3. Governing Equations for Cosmogenic Nuclides

We extended the model of Ferrier and Perron (2020) to track concentrations of cosmogenic nuclides in soil and the underlying rock (Riebe & Granger, 2013). First, we implemented TCN production in the soil and bedrock such that production rates evolve with topography. Here, we outline how the processes described above modify TCN concentrations in soil and bedrock.

To compute changes in TCN concentrations in the soil, we account for TCN production in the soil, addition of TCN from soil production, changes in TCN through the divergence of soil transport, and losses of TCN to radioactive decay and host mineral dissolution. The full expression for the change in soil TCN concentration, N_s (atoms M_{host}^{-1}), is

$$\begin{aligned}\frac{\partial N_s}{\partial t} = {} & \frac{1}{\rho_s H}\sum_{i=1}^{n} P_i(0)\Lambda_i\left(1 - e^{-\rho_s H/\Lambda_i}\right) - \frac{\rho_r C_{host,r}}{\rho_s C_{host,s}}\epsilon_0 e^{-H/H_0}(N_s - N_{r,zb}) \\ & - \frac{q_s}{H}\cdot\nabla(C_{host,s}N_s) - \lambda N_s - k_{host}A_{host}N_s\end{aligned}. \quad (8)$$

Here, i is the ith of n cosmogenic production pathways, P_i (atoms M_{host}^{-1} T^{-1}) is the cosmogenic production rate of the ith production pathway (at zero depth), and Λ_i (M L^{-2}) is the attenuation length associated with the ith production pathway. $C_{host,r}$ and $C_{host,s}$ (M M^{-1}) are the concentrations of the TCN host mineral in the bedrock and soil, respectively. $N_{r,zb}$ is the concentration of TCN at the soil-bedrock interface, and λ (T^{-1}) is the decay constant of the TCN. The last term in Equation 8 represents the loss of TCN concentration by chemical erosion, which can be ignored if the host mineral is inert or nearly so. A more complete derivation of Equation 8 can be found in Text S2 of Supporting Information S1.

In this study, we used $n = 3$ production pathways representing spallation, negative muon capture, and fast muogenic production, which is appropriate for several TCNs, including ^{10}Be, ^{26}Al, and ^{14}C in quartz (Dunai, 2010). For all production pathways, we employed the Lifton-Sato-Dunai scaling scheme (Lifton et al., 2014) within CRONUScalc (Marrero et al., 2016) using a sea-level, high-latitude ^{10}Be production rate of 3.92 atoms g_{qtz}^{-1} yr^{-1} (Borchers et al., 2016). We used Madison, Wisconsin, as a reference location to scale production rates. We obtained a uniform spallation pathway attenuation length (Λ_s) from CRONUScalc using the mean elevation of the reference model topography. To parameterize muogenic production rates and attenuation lengths, we used the codes of Balco (2017) to create 1,000 synthetic muogenic production profiles for both negative muon capture and fast production pathways across the entire range of elevations comprising our modeling runs. In keeping with previous work (Braucher et al., 2013), profiles were fitted with a single-term exponential function to arrive at a surface production rate and an attenuation length for each pathway. Similar to spallation, we used a mean attenuation length for each muogenic pathway as the range was small. We then created piecewise cubic Hermite interpolants (Fritsch & Carlson, 1980) for each production pathway using the corresponding surface production rates and elevations, allowing the model to update surface production rates as elevations change.

Calculating $N_{r,zb}$ in Equation 8 requires determining the rate of change in bedrock TCN concentration, N_r, at an arbitrary depth below the soil-bedrock interface, ξ (L), as

$$\frac{\partial N_r(\xi)}{\partial t} = \sum_{i}^{3} P_i(0)e^{-\rho_s H/\Lambda_i}e^{-\rho_r \xi/\Lambda_i} - \lambda N_r(\xi) - \epsilon_0 e^{-H/H_0}\left.\frac{\partial N_r}{\partial \xi}\right|_{\xi}. \quad (9)$$

This equation represents the sum of nuclide production in bedrock and decay while recognizing that the soil production rate history influences the bedrock nuclide concentration profile. By including deep production, periods of transient denudation rate can induce changes in the bedrock TCN concentration profile (Knudsen et al., 2019), which can alter soil TCN (Skov et al., 2019). The change in $N_{r,zb}$ is then evaluated at the soil-bedrock interface (i.e., $\xi = 0$) as

$$\frac{\partial N_{r,zb}}{\partial t} = \sum_i^3 P_i(0)e^{-\rho_s H/\Lambda_i} - \lambda N_r(\xi) - \epsilon_0 e^{-H/H_0}\frac{\partial N_r}{\partial \xi}\bigg|_{\xi=0}. \quad (10)$$

We solved an approximation of these two equations with a semi-Lagrangian advection scheme (Blackburn et al., 2018; Spiegelman & Katz, 2006) described in Section 2.4.

2.4. Inferring Denudation Rates From Cosmogenic Nuclides

To fully exploit a landscape evolution model that conserves TCN, we must be able to efficiently infer denudation rates from TCN concentrations. Throughout this study, we applied Equation 11 to infer denudation rates (D_{inf}) from N_s.

$$N_s = \sum_i^3 \frac{P_i(0)}{\lambda + D_{\text{inf}}/\Lambda_i}\left[\frac{C_{\text{host},s}}{C_{\text{host},r}}\left(1 - e^{-\rho_s H/\Lambda_i}\right) + e^{-\rho_s H/\Lambda_i}\right] \quad (11)$$

Equation 11 is nearly identical to an analogous expression from Riebe and Granger (2013) for a two-layer bedrock-soil system similar to our model; the only difference is that it includes radioactive decay. It was derived under assumptions of steady state, with constant D_{inf} and H in a well-mixed, chemically weathered soil produced from an underlying parent rock in which negligible chemical erosion occurred. Equation 11 does not have an analytical solution for D_{inf}, so in practice it must be solved numerically. Our goal is to investigate the extent to which denudation rate estimates inferred from Equation 11 would deviate from actual denudation rates during landscape transience. At all soil-mantled cells, we solved for D_{inf} in Equation 11 and others presented in Section 3 using local values of P_i, N_s, H, and $C_{\text{host},s}/C_{\text{host},r}$, all of which are measurable in the field or in the lab.

Calculators such as CRONUScalc or CRONUS solve D_{inf} from N_s numerically (Balco et al., 2008; Marrero et al., 2016). Similarly, we used model outputs of N_s, $C_{\text{host},s}$, and H to solve D_{inf} in Equation 11 as a post-processing step as it is too computationally expensive to solve at each timestep. Using a Newton-Raphson method implemented within MATLAB's variable-precision solver for Equation 11 under steady-state conditions at ridge locations not subject to downslope soil transport, D_{inf} deviates by only ~0.18% from the modeled, actual denudation rate, D_{act}.

For basin-averaged inferred denudation rate ($D_{\text{inf,basin}}$), we solved Equation 11 using a mean H and $C_{\text{host},s}/C_{\text{host},r}$, and hypsometrically averaged $P_i(0)$ for the entire basin. We did this as a post-processing step on a delineated basin through time using outputs of N_s, C_{host}, and E. We constructed a virtual stream sediment TCN concentration using these variables for all stream-side grid points. This concentration is calculated as

$$N_{s,\text{stream}} = \frac{\sum N_{s,\text{stream-side}} E_{\text{stream-side}} \rho_s C_{host,s,\text{stream-side}} \Delta x \Delta y \Delta t}{\sum E_{\text{stream-side}} \rho_s C_{host,s,\text{stream-side}} \Delta x \Delta y \Delta t}. \quad (12)$$

Here, Δx and Δy are the grid point lengths in the x and y directions, and Δt is the duration of the timestep. Thus far, few studies have accounted for enrichment or depletion of the host mineral in cosmogenic nuclide-based estimates of basin-averaged denudation rate, but recent work in carbonate landscapes underscores the importance of doing so (Ott et al., 2022, 2023). In Section 3, we show the implications of neglecting chemical erosion in point-based and basin-averaged estimates of denudation rate.

2.5. Numerical Implementation

Here, we describe some details associated with the model domain, boundary conditions, and solutions to the governing equations. In all modeling scenarios, we used a 150 × 150 regular grid with a resolution of 10 m. The boundaries of the model domain were pinned to zero elevation, allowing the boundaries to act as a regional base-level. Mass transfers to the channel network do not change the channel elevation (Ferrier & Perron, 2020). We used a timestep of 10 years to maintain an acceptable agreement between D_{act} and D_{inf} at steady state. The governing equations are solved using explicit finite difference methods. The supplement contains a detailed description of the implementation of nonlinear hillslope soil transport based on Perron (2011).

In order to solve Equations 9 and 10, we used a semi-Lagrangian advection scheme to account for deep cosmogenic production under variable denudation rates (Figure S1 in Supporting Information S1). The scheme can solve for $N_r(\xi)$ at regularly spaced depths of an evolving bedrock concentration profile (Knudsen et al., 2019). The soil production rate at a grid cell provides a vertical velocity from which we find a departure depth via cubic interpolation (Fletcher, 2019). During each timestep, TCN production rate is calculated using a depth obtained by the averaging the depth of evaluation (i.e., ξ) and the departure depth. $N_{r,zb}$ is then filled with the value at $\xi = 0$,

which is the bedrock-soil interface. The lowermost value of the profile is filled with a steady-state TCN concentration corresponding to a running average of bedrock exhumation velocities. This mimics a pre-perturbation history of TCN accumulation below the profile, which cannot be accounted for analytically. The number and spacing of evaluation points below the surface affect the accuracy of the TCN concentration relative to an analytical steady-state value due to interpolation errors (T. R. Lucas, 1974). We observed a depth of 10 m and point spacing of 10 mm to be a good compromise between accuracy and computational speed. In the supplement, we detail an alternative, speedier method for calculating $N_{r,zb}$ that does not directly track TCN profiles (Figure S2 in Supporting Information S1).

2.6. Attaining Steady-State Topography

To prepare for simulations under transient conditions (Section 4), we ran two successive simulations to obtain steady-state initial conditions. First, we generated a steady-state topography with the Tadpole landscape evolution model (Perron et al., 2008, 2009, 2012; Richardson et al., 2020). This model differs from that in Section 2 in that it includes not only soil transport but also stream incision, and in that it does not track changes in soil thickness, soil composition, or chemical erosion rate. In this model, under a threshold stream-power incision law, the change in elevation with time due to fluvial erosion is expressed as

$$\frac{\partial z}{\partial t} = \begin{cases} 0 & A^m S^n \le \theta_c \\ -K_f (A^m S^n - \theta_c) & A^m S^n > \theta_c \end{cases}, \tag{13}$$

where K_f ($L^{1-2m}\ T^{-1}$) is an effective erodibility, A (L^2) is drainage area, S is slope ($L\ L^{-1}$), m and n are unitless constants, and θ_c (L^{2m}) is an incision threshold (e.g., Pelletier, 2012; Theodoratos & Kirchner, 2020). Starting from a surface generated by red noise, we ran the model until the topography reached steady state using the same boundary conditions and model parameters used in the transient simulations (U = 50 mm kyr^{-1}, $K_{nl} = 0.0032\ m^2\ yr^{-1}$ and $S_c = 1.2$; Section 4.1) and the following values for stream incision parameters: $K_f = 0.0001\ year^{-1}$, $m = 0.5$, $n = 1$, and $\theta_c = 8$ m. We extracted the channel network from the resulting steady-state topography using a threshold drainage area of 5,000 m^2.

We then used the topography output from this first simulation as the initial condition for a second simulation with the model in Sections 2.1 and 2.2. We ran this simulation to steady state to obtain steady state values of z_s, H, C_{Xs}, and TCN concentrations. In this simulation, the channel network was fixed in the geometry it was in at the end of the Tadpole simulation. The median difference in elevation between the initial topography and the steady-state topography is ~3.5 m and is due to the inclusion of soil chemical erosion, soil production, bedrock lithology, and the fixed stream channel network.

3. Results: Steady-State TCN-Inferred Denudation Rates Are Sensitive to Soil Chemical Erosion

How do inferred denudation rates computed with Equation 11 compare to denudation rate estimates inferred from N_s via some other common formulations? Since we solved Equation 11 numerically as a post-processing step, we tracked and outputed D_{inf} by ignoring radioactive decay. If decay is neglected, Equation 11 would simplify to

$$D_{\text{inf,CEF}} = \sum_i^3 \frac{P_i(0)\Lambda_i}{N_s} \left[\frac{C_{\text{host},s}}{C_{\text{host},r}} \left(1 - e^{\rho_s H/\Lambda_i}\right) + e^{-\rho_s H/\Lambda_i} \right], \tag{14}$$

which is identical to that in Riebe and Granger (2013). Most inferred denudation rates in the literature do not correct for chemical erosion (Riebe & Granger, 2013). If chemical erosion is neglected, Equation 11 would simplify to

$$N_s = \sum_i^3 \frac{P_i(0)}{\lambda + D_{\text{inf,Lal}}/\Lambda_i}, \tag{15}$$

which is similar to that originally derived in Lal (1991) and identical to those used in denudation rate calculators when evaluating surface samples (Marrero et al., 2016) or stream sediment samples (Mudd et al., 2016). We solved Equation 15 via the same method as Equation 11.

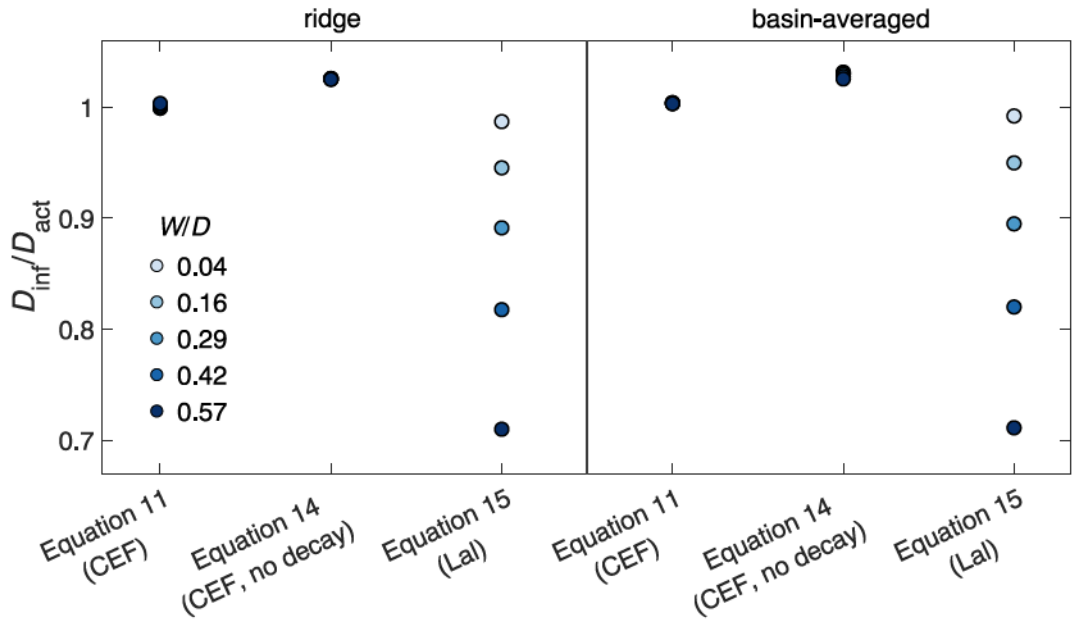

Figure 2. Ratio of inferred denudation rate (D_{inf}, computed with Equations 11, 14 and 15) to actual denudation rate, D_{act}, in steady-state landscapes at a ridge (left panel) and averaged over a small basin (right panel). Markers represent simulations with a range of ratios of chemical erosion rate to denudation rate (W/D), resulting from a range of bedrock plagioclase concentrations (5%–65%). Values of D_{inf}/D_{act} close to 1 for Equations 11 and 14 show that accounting for soil chemical erosion yields denudation rate estimates close to actual denudation rates. Values of D_{inf}/D_{act} far from 1 computed with Equation 15, which neglects chemical erosion, show that D_{inf} grows increasingly farther from D_{act} with increasing W/D. This underscores the importance of accounting for soil chemical erosion in TCN-based estimates of denudation rate. Basin-averaged rates are nearly identical to those on ridges because these simulations are steady-state landscapes.

We computed D_{inf} with Equations 11, 14, and 15 in five steady-state landscapes that differ in their bedrock concentration of the soluble phase plagioclase (5%, 20%, 35%, 50%, and 65%) and the complementary concentration of the bedrock's only other mineral phases, quartz, which is treated as insoluble (95%, 80%, 65%, 50%, and 35%, respectively). All the landscapes had a U of 50 mm kyr^{-1}. Figure 2 shows D_{inf}/D_{act} for these five landscapes using Equations 11, 14 and 15 at a ridge location not subject to downslope soil transport (left panel) and a small basin (right panel). Comparing D_{inf}/D_{act} for Equations 11 and 14 in Figure 2 shows that ignoring decay results in a small error in D_{inf} (~2.5%) in these simulations. By contrast, comparing D_{inf}/D_{act} for Equations 11 and 15 shows that neglecting the enrichment of $C_{host,s}$ by chemical erosion leads to larger errors in these simulations, up to 29% in the simulation with the highest W/D (and plagioclase concentration). These errors increase with increasing W/D, consistent with the observations in Small et al. (1999), Riebe et al. (2001), and Riebe and Granger (2013). Figure 2 also shows that the ratio diverges from 1 with increasing W/D for basin-averaged D_{inf}. In the model, the effect of W on D_{inf} is indirectly affected by U, to the extent that U affects properties like soil thickness and soluble mineral concentrations (Text S5 in Supporting Information S1).

To summarize, Figure 2 implies that calculating D_{inf} requires accounting for soil chemical depletion if the cosmogenic host mineral has a different soil residence time than the average soil material (e.g., quartz, which stays in the soil while other minerals are lost to dissolution). Our study is not the first to make this point—Small et al. (1999) and Riebe et al. (2001) did this more than 20 years ago—but our model is well-equipped to show the importance of this effect.

4. Results: Transient Landscapes

4.1. Responses to Tectonic and Climatic Perturbations

To investigate the transient response of TCN to perturbations, we performed two numerical experiments. In the first experiment, we simulated a simple tectonic perturbation in which initially steady-state landscape experiences an instantaneous doubling of rock uplift rate (or equivalently a doubling of the lowering rate of the domain boundaries and the channels) from 50 mm kyr^{-1} to 100 mm kyr^{-1}. In the second experiment, we simulated a

Table 1
Model Parameters for Transient Perturbation Experiments

Model parameter	Tectonic	Climatic
Δt—model timestep	10 yr	10 yr
Δx, Δy—grid resolution	10 m	10 m
U—bedrock uplift rate	0.05 to 0.1 mm yr^{-1}	0.05 mm yr^{-1}
K_{nl}—hillslope transport efficiency (nonlinear)	0.0032 m^2 yr^{-1}[a]	0.0032–0.0048 m^2 yr^{-1}
S_C—critical hillslope gradient	1.2 m m^{-1}[b]	1.2 m m^{-1}
ϵ_0—maximum soil production rate	0.268 mm yr^{-1}[c]	0.268–0.402 mm yr^{-1}
H_0—soil production rate scaling length	1/3 m[c]	1/3 m
ρ_s—soil density	1,325 kg m^{-3}	1,325 kg m^{-3}
ρ_r—bedrock density	2,650 kg m^{-3}	2,650 kg m^{-3}
k_{plag}—plagioclase dissolution rate constant	0.000005 mol m^{-2} yr^{-1}[d]	0.000005–0.0000075 mol m^{-2} yr^{-1}
A_{plag}—plagioclase mineral specific surface area	117 m^2 mol^{-1}[d]	117 m^2 mol^{-1}
ξ_{max}—max depth of bedrock concentration profile	10 m	10 m
ξ spacing—distance between profile evaluation points	0.01 m	0.01 m
# averaging timesteps for cosmogenic profile infilling	20,000	20,000

[a]Roering et al. (1999). [b]Roering et al. (2001). [c]Heimsath et al. (2001). [d]Ferrier and Kirchner (2008) and Clow and Drever (1996).

simple climatic perturbation in which the maximum soil production rate, hillslope transport efficiency, and the dissolution rate constant of plagioclase were simultaneously increased by 50%. This tests the response of TCN to a "top-down" perturbation where the entirety of the hillslope area is affected at the same time (Mudd, 2017). In both experiments, we restricted our attention to the responses of the hillslopes by fixing the lateral position of the stream network in place during the simulation (Hurst et al., 2012; Mudd & Furbish, 2007). In each simulation, we ran the model until C_{Xs}, H, and N_s reached new steady-state values, which occurred at 3 and 3.1 Myr of model run time in the tectonic and climatic experiments, respectively.

To quantify the difference between the actual instantaneous denudation rate D_{act} and the TCN-based estimate of denudation rate D_{inf} (Equation 11), we introduce the metric $D_{diff} = D_{inf} - D_{act}$. This reveals the magnitude of the error in the TCN-inferred denudation rate and is a measure of the deviation from steady-state conditions in a non-steady landscape. This can be calculated at any point on the landscape, and therefore can reveal spatial patterns in deviations from steady state. It can also be calculated for a drainage basin as the difference between the basin-averaged inferred denudation rate, $D_{inf,\,basin}$, and the actual basin-averaged denudation rate, $D_{act,\,basin}$.

In both experiments, the initial U is 50 mm kyr^{-1}. All model parameters used in the perturbation experiments are listed in Table 1. We use values of K_{nl}, S_c, and ϵ_0 from the Oregon Coast Range as it is one of the few landscapes where these parameters have been calibrated from field measurements (Heimsath et al., 2001; Roering et al., 1999). The k_{plag} parameter comes from the field measurements of Clow and Drever (1996). Both scenarios are assigned the same bedrock mineralogy (50% plagioclase and 50% quartz) to simplify the interpretation of soil composition in terms of one easily weathered phase and one insoluble phase.

The responses of landscape-wide D_{inf} and D_{act} differed spatially and temporally between the two experiments. In the tectonic scenario, the areas around channels responded first to the increase in uplift rate, steepening and increasing D_{act}. This was followed by a wave of increased physical erosion rate that gradually propagated up the hillslopes to the ridges (Figure 3). Although D_{act} exhibited notable change around channels by 100 kyr, D_{inf} showed little change (Figure 3). This is due to downslope soil transport from upslope areas that have not yet reached the new steady-state conditions, which buffers the response in convergent hollows and footslopes. Both D_{act} and D_{inf} along ridges equilibrated slowly to the perturbation. D_{inf} stayed close to local steady state ($D_{inf} \approx D_{act}$) on ridges throughout the experiment, such that the minimum D_{diff} stayed above -10 mm kyr^{-1}. By comparison, D_{diff} on footslopes and hollows was larger and persisted due to the buffering effect of hillslope transport (Figure 3). Across the entire experiment, D_{inf} deviated from D_{act} by at most 64% during the experiment ($D_{diff} = -46$ mm kyr^{-1}), which occurred at 71 kyr in hollows directly above channel heads and along channels below long hillslopes. Positive D_{diff} values were low ($D_{diff} = 3$ mm kyr^{-1}) during the entirety of the experiment, implying that D_{inf} did not exceed D_{act} by much at any time or place.

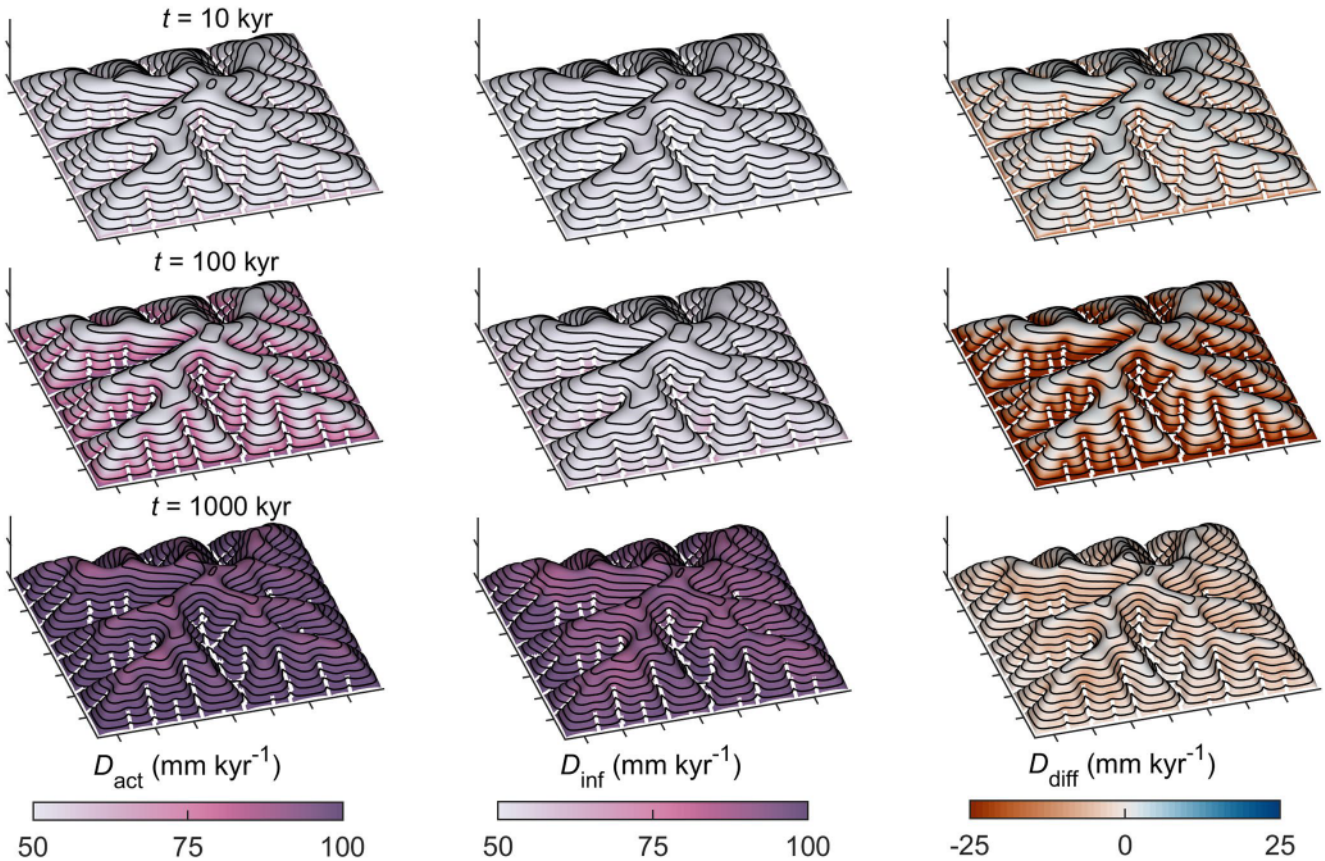

Figure 3. Landscape distributions of actual and inferred denudation rates D_{act} and D_{inf} (Equation 11), and the difference $D_{diff} = D_{inf} - D_{act}$ for the tectonic experiment at 10, 100, and 1,000 kyr after the perturbation. Topography shown at 2x vertical exaggeration. The model domain is 1.5 km by 1.5 km. Topographic contours are every 15 m. Maximum elevation is 180 m at 1,000 kyr. A movie of the experiment is available as a supplement (Movie S1). Ridges not subject to hillslope soil transport remain near local steady state ($D_{inf} \approx D_{act}$) throughout the simulation.

Closer investigation of changes in H, N_s, and C_{Xs} at different hillslope positions through time showed how large D_{diff} developed in hollows and footslopes through the transport of N_s and C_{Xs} (Figure 5b–5e). In the hollows, the decrease in H far outpaced the slower response of N_s and C_{Xs}. This suggests that estimates of D_{inf} inferred from samples on ridges (Ferrier et al., 2012; Larsen et al., 2014) should be good indicators of current D_{act} during tectonic-style perturbations like the one imposed here. At the ridge, larger magnitude changes in U induced larger D_{diff} that equilibrated faster due to hillslope steepening and soil thinning as the landscape approached S_C (Figure S3 in Supporting Information S1).

Across the landscape in the climatic experiment, D_{act} increased rapidly after the initial perturbation, and D_{inf} increased nearly as rapidly. This resulted in negative D_{diff} values at 10 kyr (Figure 4). D_{inf} and D_{act} attained a mean maximum difference of around 44% ($D_{diff} = -21$ mm kyr^{-1}) across all hillslope positions at 2 kyr. By 100 kyr, stream channel incision rate started to dominate the response, and a wave of decreased D_{act} migrated upslope, which generated positive D_{diff} (Figure 4). This was again due to the buffering capacity of soil transported from hillslope positions at different stages of transient evolution. When N_s, C_{Xs}, and H from different hillslope positions are considered, the perturbation to ϵ_0, soil production efficiency, rapidly increased H at all positions, which resulted in a decrease in N_s. The relatively fast change in these variables explains the quick recovery of D_{diff} to near zero (Figures 5g and 5h). As the channels began to dominate, the hillslope positions displayed differing responses. Soil transport delayed the recovery to steady-state conditions by supplying Ns and C_{Xs} from ridges to footslopes and hollows, leading to prolonged positive D_{diff} in these locations (Figures 5g and 5h). Given these results, perturbations that synchronously disrupt the entire landscape may cause inaccuracies in real-world estimates of D_{inf} on ridges directly after the perturbation. These inaccuracies would grow and be prolonged if the magnitude of the perturbation change were increased (Figure S4 in Supporting Information S1).

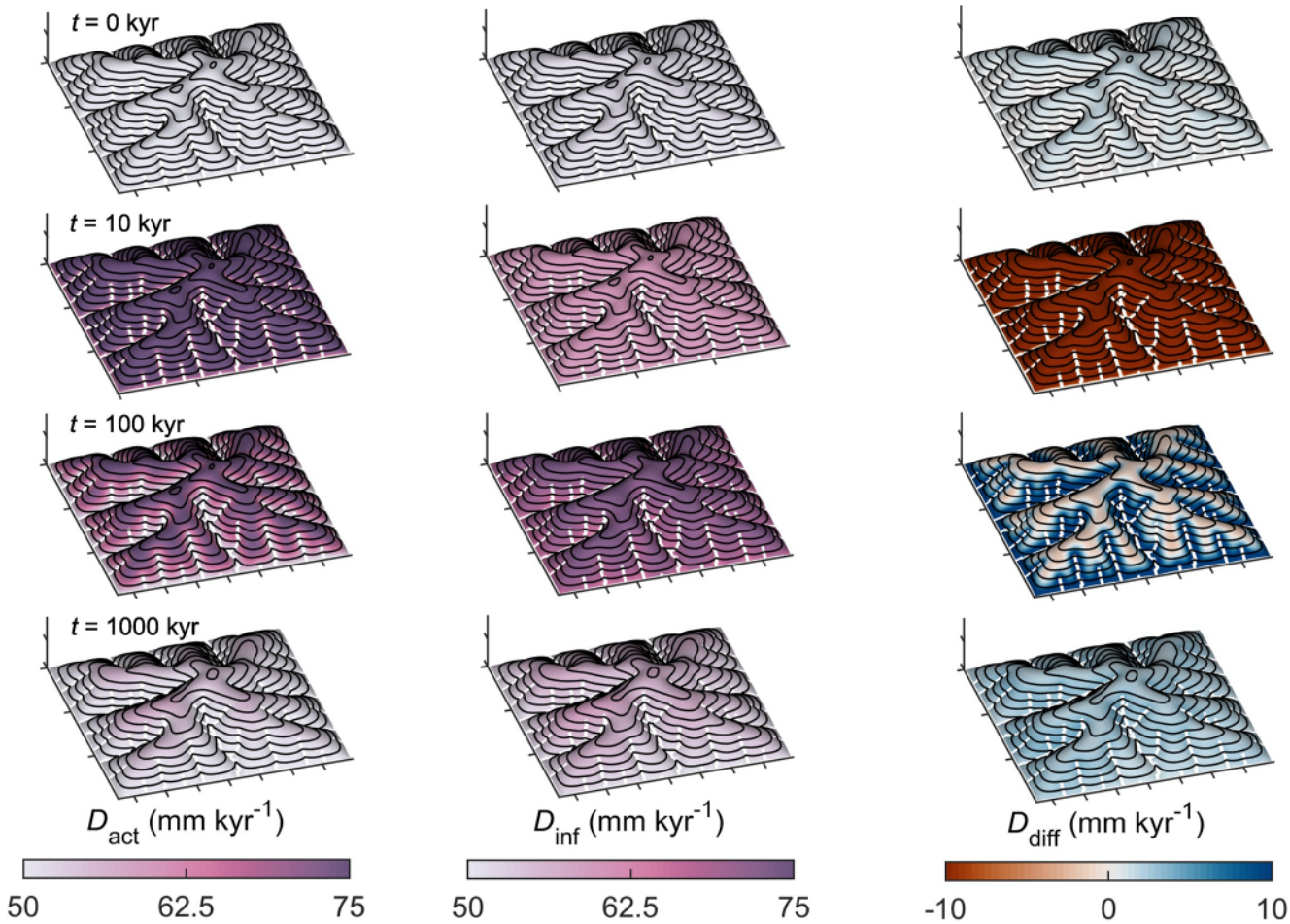

Figure 4. Landscape distributions of actual and inferred denudation rates D_{act} and D_{inf} (Equation 11), and the difference $D_{diff} = D_{inf} - D_{act}$ for the climatic experiment at 0, 10, 100, and 1,000 kyr after the perturbation. Topography shown with 2x vertical exaggeration. The model domain is 1.5 km by 1.5 km. Contours are every 15 m. The maximum elevation is 135 m at 1,000 kyr. A movie of the experiment is available as a supplement (Movie S2). The initial surfaces ($t = 0$ kyr) illustrate the abrupt initial change in all variables during this experiment. For this type of perturbation, D_{diff} varies between negative and positive values depending on the time since perturbation and hillslope position.

Figure 6 shows $D_{diff, basin}$, the difference between the basin-averaged TCN-inferred denudation rate, $D_{inf, basin}$, and the basin-averaged instantaneous denudation rate, $D_{act, basin}$, for the drainage basin outlined in Figure 6. $D_{diff, basin}$ was relatively small throughout most of each simulation, yet the time series of $D_{diff, basin}$ differed in style between the tectonic and climatic experiments. In the tectonic experiment, $D_{diff, basin}$ progressed to -7 mm kyr^{-1} (10% difference) at ~158 kyr and then declined gradually to nearly zero over ~1 Myr (Figure 6b). In contrast, in the climatic experiment, $D_{diff, basin}$ evolved as a sharp initial pulse to a maximum of -23 mm kyr^{-1} (37% difference) at 2 kyr and then returned to near zero within 83 kyr (Figure 6c), a much faster response than that in the tectonic experiment. This was followed by a longer, lower-amplitude response in which $D_{diff, basin}$ grew as large as 2 mm kyr^{-1} and then decayed to nearly zero over ~1 Myr, similar to the duration of the response in the tectonic experiment (Figure 6b). Larger magnitude changes in the perturbed parameters for each scenario generated greater $D_{diff, basin}$ which equilibrated either more rapidly (tectonic) or slowly (climatic) due to steeper (tectonic) or gentler (climatic) gradients (Figures S5 in Supporting Information S1).

The results show that these transient changes in bedrock uplift rate, soil production rate, dissolution rate, and soil transport rate do not generate large errors in estimates of $D_{inf, basin}$ from TCN in stream sediment. This implies that large errors in $D_{inf, basin}$ in practice are more likely to arise from processes not represented in the model, such as deep-seated landslides (Schide et al., 2022; Yanites et al., 2009) or sediment storage along or within the stream network (Grischott et al., 2017). The inclusion of dynamic channels would increase the response time in the tectonic scenario since the response would need to transit the channel network before propagating through the hillslopes (Hurst et al., 2012).

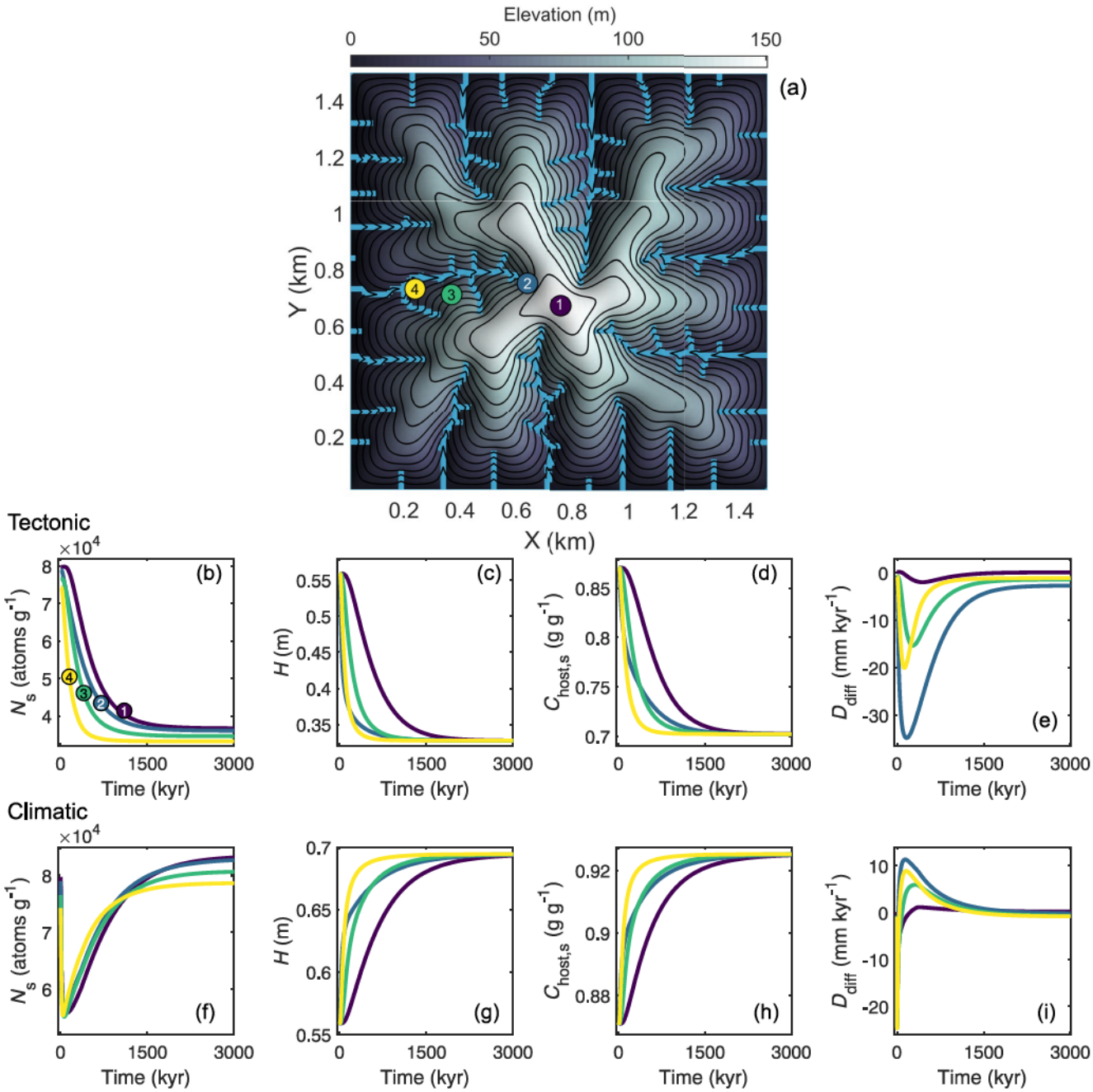

Figure 5. (a) Map view of the initial topography for the tectonic and climatic perturbation experiments. Channels marked in blue. Numbers 1–4 indicate the hillslope positions (1: ridge; 2: channel head; 3: sideslope; and 4: near-channel) that are tracked in panels (b–i). (b–e) Time-series plots of N_s, H, $C_{host,s}$, and D_{diff} from tectonic perturbation experiment. (f–i) Time series plots from climatic perturbation. Initial variability in N_s is due to hillslope soil transport. The variable responses show that hillslope position determines how the underlying variables used to obtain D_{inf} evolve.

4.2. Response Times

The time it takes a landscape to respond to external forcings is a fundamental property of the landscape. This response time is useful because it can be compared to time scales of climatic or tectonic forcings and used to identify whether a landscape is likely to be close to steady state (e.g., Roering et al., 2001). Here we use the tectonic and climatic experiments in Figures 3 and 4 to calculate response times of several characteristics of the landscape (soil TCN concentrations, soil thickness, soil mineralogy, and denudation rates). To do this, we applied a modified version of the response time calculation in Ferrier and Perron (2020), adapted to accommodate variables with

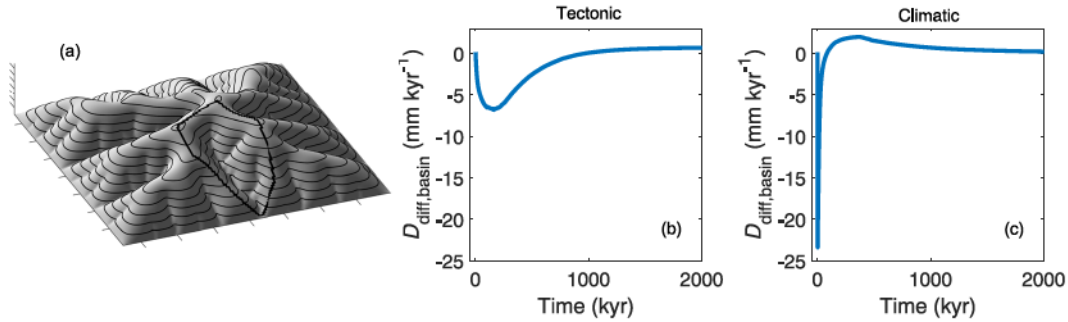

Figure 6. (a) Initial topography with selected basin outlined in black. (b) Difference between inferred and actual basin-averaged denudation rates, $D_{\text{diff, basin}}$, for the initial 2,000 kyr of modeling time in the tectonic experiment. During this simulation, errors in $D_{\text{inf, basin}}$ were no larger than 7 mm kyr^{-1}, damped by the range of cosmogenic nuclide production rates within the basin and through the collection of an integrated sediment sample. (c) The climatic experiment shows that $D_{\text{diff, basin}}$ could be large directly after a perturbation but recover relatively rapidly given a constant tectonic regime.

similar initial and final values (e.g., for D_{act} and D_{inf} in the climatic experiment in Figure 5). For instance, for D_{inf}, we define the response time as the time it takes D_{inf} to get 95% of the way to its new steady-state value relative to the maximum deviation of D_{inf} from its new steady-state value. In mathematical terms, this is the time at which D_{inf} first satisfies the condition $|D_{\text{inf}} - D_{\text{inf, final}}| < \max(0.05|D_{\text{inf},t} - D_{\text{inf, final}}|)$ and continues to satisfy it for the remainder of the simulation. Here, $D_{\text{inf},t}$ is the entire time series of D_{inf} for the modeling run, $D_{\text{inf, final}}$ is the final steady-state value of D_{inf}, and 0.05 is a 5% threshold level. The response time is defined this way for every point in the landscape. We used this definition to calculate the response time, τ, for N_s, H, $C_{\text{host},s}$, D_{act}, and D_{inf}, which we denote τ_{Ns}, τ_H, $\tau_{\text{Chost},s}$, $\tau_{D\text{act}}$, and $\tau_{D\text{inf}}$, respectively.

When response times are mapped across the landscape, they reveal spatial patterns in the propagation of signals throughout the domain. Figure 7 shows that response times varied between the tectonic and climatic experiments and among variables within each experiment. In the tectonic experiment, the response time of D_{inf} was greater than the response times of all other variables. τ_{Dinf} varied in space across the landscape from 368 kyr to 1.735 Myr and had a mean (± s.d.) of 1.304 Myr ± 223 kyr (Figure 7f). For the variables not associated with cosmogenic nuclides, areas near channels responded fastest (e.g., τ_H and $\tau_{D\text{act}}$ in Figures 7b and 7e). However, τ_{Dinf} was high along channels where hillslope sediment transport from ridges carried down parcels of soil with higher N_s (Figure 7f). Ridges responded slower than other parts of the landscape for every characteristic (Figure 7a–7f), mimicking the way the perturbation in bedrock uplift is translated upslope (Mudd & Furbish, 2007). When this experiment is viewed holistically, the redistribution of relict N_s downslope controls the response time of D_{inf}.

Response times in the climatic experiment were longer than those in the tectonic experiment for all variables (Figure 7g–7l). This differs from a similar experiment in Ferrier and Perron (2020) and is likely due to the introduction of more complex topography and different parameter values. The mean (± s.d.) of τ_{Dinf} in the climatic experiment was 1.604 Myr ± 276 kyr and varied from 784 kyr to 2.238 Myr. High τ_{Dinf} in top-central area of the modeling domain is indicative of topographic control on τ_{Dinf} (Figure 7l). This zone underwent the most topographic adjustment during the perturbation. These response times show that relatively small perturbations in the efficiencies of hillslope processes could lead to transient states lasting much longer than the timescale of climatic fluctuations. Although this is the case, as shown in Figures 5 and 6, D_{diff} on ridges is quite low for the vast duration of modeling time. This means that even though τ_{Dinf} is high for perturbations affecting climate-related hillslope processes, D_{inf} values should reflect D_{act} at almost any point in time except for directly after the onset of a step-change.

5. Discussion

5.1. Sensitivity of Response Times for Maximum D_{diff} and D_{inf} to Hillslope Length

Hillslope length (L_h) is a fundamental landscape property and is defined as the distance from ridges to stream channels (Grieve et al., 2016). Numerical modeling and experimental work have shown that L_h is set by the competition between advective fluvial processes and diffusive hillslope processes (Perron et al., 2009; Sweeney

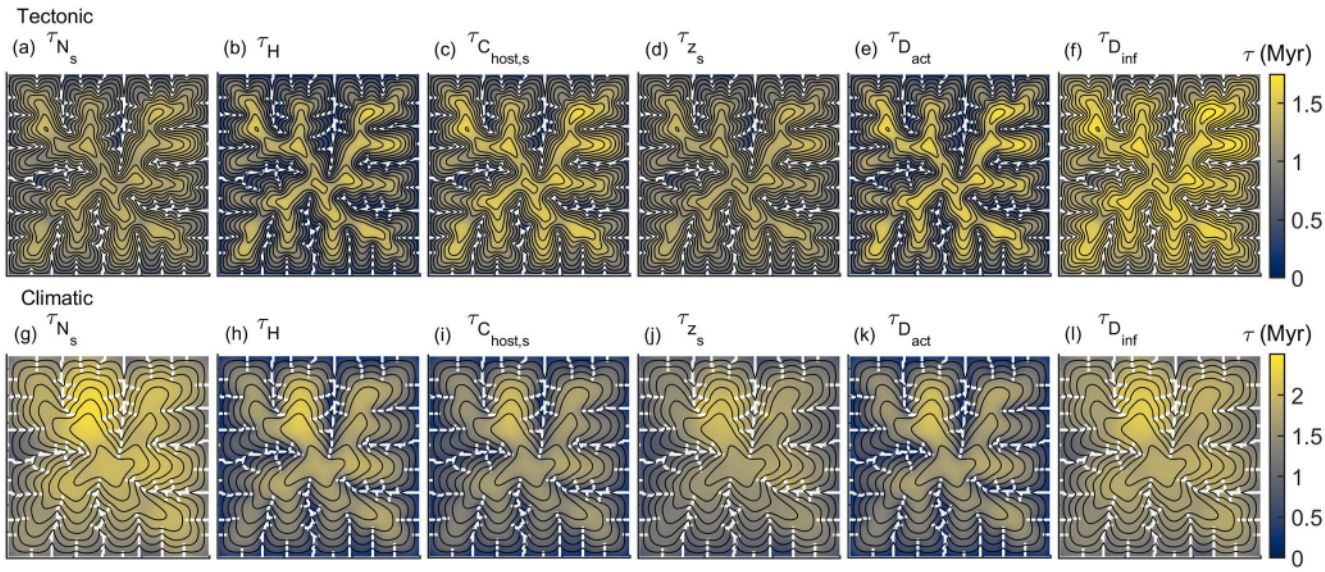

Figure 7. (a–l) Response times (τ) of soil cosmogenic nuclide concentration (N_s), soil thickness (H), cosmogenic nuclide host mineral concentration ($C_{host,s}$), actual denudation rate (D_{act}), and inferred denudation rate (D_{inf}) for the tectonic (a–f) and climatic experiments (g–l) (Figures 3 and 4). The response time of D_{inf} is longest on ridges due to the combined response times of all the underlying variables, but, as the text details, the deviation of D_{inf} from D_{act} is smallest on ridges.

et al., 2015). In numerical simulations in Ferrier and Perron (2020), chemical erosion rates took longer to respond to perturbations in landscapes with longer hillslopes. This matches previous modeling of topographic response times of a single hillslope for both linear and nonlinear hillslope sediment transport to changes in bedrock uplift (Fernandes & Dietrich, 1997; Roering et al., 2001). These studies suggest that L_h should influence cosmogenic nuclide behavior as well, including response times and the magnitude of D_{diff}.

To test the sensitivity of the maximum D_{diff} ($D_{diff,max}$) and D_{inf} response time (τ_{Dinf}) to L_h in our model, we generated four synthetic landscapes with a range of L_h values. We generated these using the previously mentioned stream power incision model and applied the same parameters as in the numerical experiments in Figures 3–5 except for K_f (effective erodibility) and the drainage area threshold for channel extraction. This yielded four landscapes that had average L_h values ranging from 34.5 to 93.2 m. With these landscapes, we explored the sensitivity of $D_{diff,max}$ and τ_{Dinf} to L_h by applying the same tectonic-style perturbation to each of them, which involved a step-change in bedrock uplift rate from 50 mm kyr^{-1} to 100 kyr^{-1}, as shown in Figure 4. To demonstrate spatial variations in the responses within each landscape, we computed $D_{diff,max}$ at multiple hillslope positions (ridge, sideslope, channel head) and as a basin-averaged quantity in a small basin in each simulation.

The landscape position at which D_{inf} deviated the least from D_{act} was on ridges. Figure 8a shows that this was the case at all average hillslope lengths and that the magnitude of the deviation of D_{inf} from D_{act} decreased with L_h. In contrast, the largest deviations of D_{inf} from D_{act} occurred at channel heads, where the largest deviations were temporarily greater than the imposed change in uplift rate at the beginning of the simulation.

The patterns of $D_{diff,max}$ are instructive. Because ridges respond last to base-level perturbations, they are the parts of the landscape where D_{inf} most closely tracks D_{act}, making them ideal sampling locations for measuring physical and chemical erosion rates (Ferrier et al., 2016). This is particularly so above long hillslopes, where the difference between D_{inf} and D_{act} approaches zero (Figure 8a). However, in landscapes with ridge-visiting landslides (Campforts et al., 2022; Dahlquist et al., 2018), this agreement between D_{inf} and D_{act} could be violated. Similar to the ridges, basin-averaged D_{inf} better depicts basin-averaged D_{act} as L_h increases, as the method considers nuclide production rates throughout the basin, including slowly responding areas (Granger et al., 1996; Mudd et al., 2016). Channel heads and sideslopes produced greater $D_{diff,max}$ with increasing L_h due to enhanced buffering of D_{inf} by hillslope transport of relatively high N_s soil from the slowly responding ridges.

τ_{Dinf} increased with L_h at all topographic positions and was largest at ridges (Figure 8b). Landscapes with longer hillslopes exhibited shorter basin-averaged τ_{Dinf} relative to the sideslope and channel head. This is due to lower final steady-state D_{inf} from downslope transport from ridges to these positions, which makes meeting the response

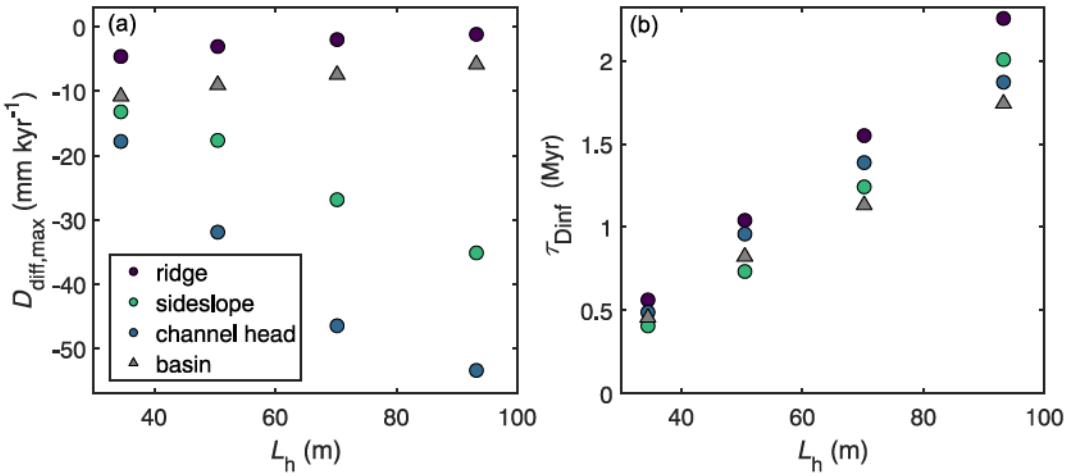

Figure 8. (a) Maximum difference between the cosmogenic ^{10}Be-inferred and actual denudation rates ($D_{diff,max}$) during simulations in which rock uplift rate instantaneously increases. (b) Response times of inferred denudation rate (τ_{Dinf}) to a step-change in bedrock uplift rate from 50 to 100 mm kyr^{-1} on landscapes with different average hillslope lengths (L_h). The ridge, sideslope, and channel head points are specific, manually selected hillslope positions similar to those in Figure 5. The basin-averaged points correspond to small basins similar to that in Figure 6.

criterion more demanding. At the longest L_h, the channel head τ_{Dinf} is lower than the sideslope because D_{inf} at the channel head goes down by ~5 mm kyr^{-1}, easing the satisfaction of the response criterion. Response times were also sensitive to U, with faster responses at higher U (Figure S3 in Supporting Information S1).

5.2. Detection of Transience in a Small Catchment Directly With One Cosmogenic Nuclide

Recognition of ongoing topographic change at the scale of headwater streams can be challenging. Testing theoretical concepts in fluvial and hillslope geomorphology often begins by assuming a condition of topographic steady state (Dietrich et al., 2003). A test of transience using cosmogenic nuclides could eliminate concerns over this confounding factor when formulating geomorphic transport laws relating mass fluxes to landscape properties.

Recently, Mudd (2017) highlighted that at the scale of a soil profile (experiencing no soil transport from upslope) one cannot detect instantaneous removals of overlying material or step-changes in denudation rate using single cosmogenic nuclide depth-profile sampling. This condition can be overcome by using a radionuclide pair such as in situ ^{14}C/^{10}Be, where one nuclide decays much more rapidly (Hippe, 2017). Using this technique, changes in the magnitude and timing of denudation rate can be identified for perturbations occurring in the last several thousand years (e.g., anthropogenic change) (Hippe et al., 2019). Due to its fast decay rate, in situ-produced ^{14}C is only moderately responsive to changes in D_{act} in the 30 mm kyr^{-1} to 100 mm kyr^{-1} range (Skov et al., 2019), which is a common range in soil-mantled uplands (Dixon & von Blanckenburg, 2012).

Our results show that detection of basin-scale transience due to changes in U could be feasible through systematic sampling using one nuclide. Divergent hillslopes close to the channel respond rapidly to the change (Figure 9a). If a low ridge and a higher ridge above it were sampled in the same basin, measured D_{inf} values on these ridges would differ markedly during transience, potentially beyond commonly reported analytical uncertainties (10%). In Figure 9a, the difference between these D_{inf} curves is labeled as a "transience detection window." The difference in D_{inf} values corresponds to the current magnitude of transience, but both the future steady-state D_{act} and the time since the perturbation would be indeterminate. The maximum magnitude of the difference and the duration of this transience detection window would scale with the length of the hillslope below the sampled ridge. This suggests that measuring N_s on low and high ridges within a given basin may provide a constraint on the current magnitude of basin-scale landscape transience. These could be paired with topographic analysis of knickpoints (Neely et al., 2017) and stream network disequilibrium between neighboring basins (Willett et al., 2014) to obtain a more complete picture of a landscape's deviation from steady state.

In contrast, no analogous transience detection window appeared in the climatic perturbation experiment due to the synchronous response across the landscape (Figure 9b). Instead, values of D_{inf} on different ridges agreed with

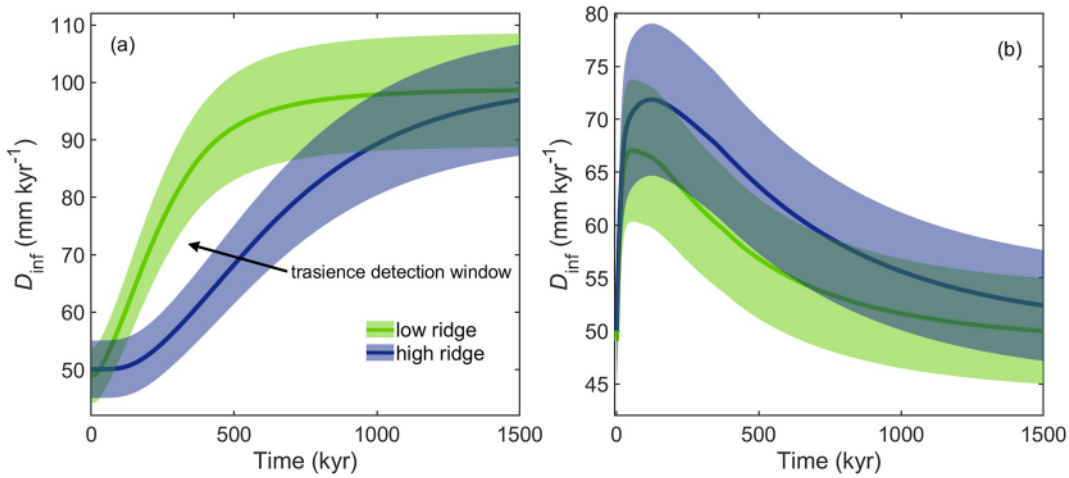

Figure 9. (a) Cosmogenic ^{10}Be-inferred denudation rate D_{inf} at two hillslope positions—one at a high-elevation ridge, the other at a low-elevation ridge—in a simulation undergoing a step change in rock uplift rate from 50 to 100 mm kyr^{-1} at $t = 0$ kyr. The uncertainty bounds are ±10% on N_s and are meant to show how D_{inf} values could be distinguished from one another in practice. The transience detection window exists for around ~700 kyr in this case. As both the high-ridge and low-ridge D_{inf} are near D_{act} during the entire perturbation, the gap between the low ridge and high ridge would indicate the current magnitude of transience but not the final D_{act} at steady state. (b) Same but for a step change in climatic parameters, which does not exhibit a detection window.

one another within uncertainty throughout this simulation. This suggests that detecting long-lived changes in D_{act} arising from changes in hillslope soil transport efficiency may require sedimentary record-based paleo-denudation rates (Marshall et al., 2017).

6. Conclusions

We used our newly introduced landscape evolution model to compute changes in soil cosmogenic nuclide concentrations alongside simultaneous changes in topography, soil thickness, and soil composition stemming from idealized tectonic and climatic perturbations. Our simulations highlighted several key conclusions.

First, accounting for the effects of chemical erosion on soil quartz enrichment is necessary for accurately inferring denudation rates in weathered soils (Figure 2). This supports previous work by Small et al. (1999), Riebe et al. (2001), and Riebe and Granger (2013). It also suggests that soil chemical erosion may explain some of the scatter in compilations of TCN-based denudation rates (e.g., Portenga & Bierman, 2011) and thus may help resolve climatic, lithologic, tectonic, and topographic controls on landscape evolution (e.g., Kirchner & Ferrier, 2013; Larsen et al., 2014; Perron, 2017; Willenbring et al., 2013).

Second, tectonic perturbations produce spatiotemporal variations in D_{inf} that differ from those induced by climatic perturbations (Figures 3–5). This suggests that spatial and temporal patterns in TCN-based denudation rate estimates are useful indicators of the drivers of past changes in topography and sediment fluxes.

Third, estimates of basin-averaged D_{inf} closely track actual basin-averaged denudation rates at most times during these simulations, with D_{inf} differing from D_{act} by less than ~10% for the entire tectonic experiment (Figure 6). The exception to this is a brief excursion after the climatic perturbation in Figure 5, when D_{act} changed immediately everywhere across the landscape, while D_{inf} took ~15 kyr to adjust. This implies that TCN-based estimates of basin-averaged denudation rate should be a reliable reflection of actual denudation rates in transient landscapes, except shortly after perturbations that affect the entire landscape at once. This supports early studies that validated the use of TCN to infer basin-averaged denudation rates (Bierman & Steig, 1996; Brown et al., 1995; Granger et al., 1996), which noted that mixing of stream sediment should strongly damp within-basin variations in TCN, and therefore that well-mixed stream sediment should have TCN concentrations that closely match the basin-average TCN concentration.

Fourth, the response times of D_{inf} to climatic and tectonic perturbations are long (~10^5–10^6 years) and increase with hillslope length (Figures 7 and 8). This implies that the response times of D_{inf} should be influenced by the

climatic, biological, and lithologic processes that control the efficiencies of river incision and soil transport and hence hillslope length (Perron et al., 2009, 2012; Richardson et al., 2019). This in turn raises the possibility that the primary influences of life, climate, and rock type on denudation rate may not be on the magnitude of denudation rate, but rather on the duration and spatial pattern of its responses to perturbations.

Lastly, in landscapes that are still adjusting to a past perturbation, it may be possible to quantify the degree to which the landscape deviates from steady state. For example, measuring a single TCN in two ridgetop soils within a single basin can yield the current magnitude of topographic transience after a simple tectonic perturbation (Figure 9). Since ridges tend to have D_{inf} that most closely track D_{act}, sampling ridges rather than other landscape positions may yield the clearest picture of this transient evolution.

Together, these results illustrate the ways in which this model can be used to investigate the coupled evolution of topography, soil chemistry, and cosmogenic nuclide concentrations. The model will be a useful tool for exploring the controls on TCN in soil and stream sediment in transient landscapes, and this in turn can help improve interpretations of denudation rate estimates derived from field measurements of TCN.

Data Availability Statement

MATLAB code to run the model and initial conditions for featured model runs are available from the Zenodo repository (Reed et al., 2023, https://doi.org/10.5281/zenodo.8256787). Model output files for the two numerical experiments are large (>5 GB) but are available upon request from the corresponding author.

Acknowledgments
We would like to thank Simon Mudd and Sean Gallen for their reviews that greatly improved the manuscript. We would also like to thank Associate Editor Jon Pelletier for his insightful comments. This work was supported by NSF Grant EAR 2045433 to KLF.

References

Anderson, R. S. (2015). Particle trajectories on hillslopes: Implications for particle age and ^{10}Be structure. *Journal of Geophysical Research: Earth Surface*, *120*(9), 1626–1644. https://doi.org/10.1002/2015JF003479

Balco, G. (2017). Production rate calculations for cosmic-ray–muon-produced ^{10}Be and ^{26}Al benchmarked against geological calibration data. *Quaternary Geochronology*, *39*, 150–173. https://doi.org/10.1016/j.quageo.2017.02.001

Balco, G., Stone, J. O., Lifton, N. A., & Dunai, T. J. (2008). A complete and easily accessible means of calculating surface exposure ages or erosion rates from ^{10}Be and ^{26}Al measurements. *Quaternary Geochronology*, *3*(3), 174–195. https://doi.org/10.1016/j.quageo.2007.12.001

Beeson, H. W., McCoy, S. W., & Keen-Zebert, A. (2017). Geometric disequilibrium of river basins produces long-lived transient landscapes. *Earth and Planetary Science Letters*, *475*, 34–43. https://doi.org/10.1016/j.epsl.2017.07.010

Bierman, P., & Steig, E. J. (1996). Estimating rates of denudation using cosmogenic isotope abundances in sediment. *Earth Surface Processes and Landforms*, *21*(2), 125–139. https://doi.org/10.1002/(sici)1096-9837(199602)21:2<125::aid-esp511>3.0.co;2-8

Blackburn, T., Ferrier, K. L., & Perron, J. T. (2018). Coupled feedbacks between mountain erosion rate, elevation, crustal temperature, and density. *Earth and Planetary Science Letters*, *498*, 377–386. https://doi.org/10.1016/j.epsl.2018.07.003

Borchers, B., Marrero, S., Balco, G., Caffee, M., Goehring, B., Lifton, N., et al. (2016). Geological calibration of spallation production rates in the CRONUS-Earth project. *Quaternary Geochronology*, *31*, 188–198. https://doi.org/10.1016/j.quageo.2015.01.009

Braucher, R., Bourlès, D., Merchel, S., Romani, J. V., Fernadez-Mosquera, D., Marti, K., et al. (2013). Determination of muon attenuation lengths in depth profiles from in situ produced cosmogenic nuclides. *Nuclear Instruments and Methods in Physics Research Section B: Beam Interactions with Materials and Atoms*, *294*, 484–490. https://doi.org/10.1016/j.nimb.2012.05.023

Braun, J., Heimsath, A. M., & Chappell, J. (2001). Sediment transport mechanisms on soil-mantled hillslopes. *Geology*, *29*(8), 683–686. https://doi.org/10.1130/0091-7613(2001)029<0683:stmosm>2.0.co;2

Brown, E. T., Stallard, R. F., Larsen, M. C., Raisbeck, G. M., & Yiou, F. (1995). Denudation rates determined from the accumulation of in situ-produced ^{10}Be in the Luquillo Experimental Forest, Puerto Rico. *Earth and Planetary Science Letters*, *129*(1–4), 193–202. https://doi.org/10.1016/0012-821x(94)00249-x

Campforts, B., Shobe, C. M., Overeem, I., & Tucker, G. E. (2022). The art of landslides: How stochastic mass wasting shapes topography and influences landscape dynamics. *Journal of Geophysical Research: Earth Surface*, *127*(8), e2022JF006745. https://doi.org/10.1029/2022jf006745

Clow, D. W., & Drever, J. I. (1996). Weathering rates as a function of flow through an alpine soil. *Chemical Geology*, *132*(1–4), 131–141. https://doi.org/10.1016/s0009-2541(96)00048-4

Codilean, A. T., Munack, H., Saktura, W. M., Cohen, T. J., Jacobs, Z., Ulm, S., et al. (2022). OCTOPUS database (v. 2). *Earth System Science Data*, *14*(8), 3695–3713. https://doi.org/10.5194/essd-14-3695-2022

Dahlquist, M. P., West, A. J., & Li, G. (2018). Landslide-driven drainage divide migration. *Geology*, *46*(5), 403–406. https://doi.org/10.1130/g39916.1

Dalca, A. V., Ferrier, K. L., Mitrovica, J. X., Perron, J. T., Milne, G. A., & Creveling, J. R. (2013). On postglacial sea level—III. Incorporating sediment redistribution. *Geophysical Journal International*, *194*(1), 45–60. https://doi.org/10.1093/gji/ggt089

Dietrich, W. E., Bellugi, D. G., Sklar, L. S., Stock, J. D., Heimsath, A. M., & Roering, J. J. (2003). Geomorphic transport laws for predicting landscape form and dynamics. *Geophysical Monograph-American Geophysical Union*, *135*, 103–132.

Dixon, J. L., & von Blanckenburg, F. (2012). Soils as pacemakers and limiters of global silicate weathering. *Comptes Rendus Geoscience*, *344*(11–12), 597–609. https://doi.org/10.1016/j.crte.2012.10.012

Dunai, T. J. (2010). *Cosmogenic nuclides: Principles, concepts and applications in the Earth surface sciences*. Cambridge University Press. https://doi.org/10.1017/CBO9780511804519

Fernandes, N. F., & Dietrich, W. E. (1997). Hillslope evolution by diffusive processes: The timescale for equilibrium adjustments. *Water Resources Research*, *33*(6), 1307–1318. https://doi.org/10.1029/97wr00534

Ferrier, K. L., Austermann, J., Mitrovica, J. X., & Pico, T. (2017). Incorporating sediment compaction into a gravitationally self-consistent model for ice age sea-level change. *Geophysical Journal International*, *211*(1), 663–672. https://doi.org/10.1093/gji/ggx293

Ferrier, K. L., & Kirchner, J. W. (2008). Effects of physical erosion on chemical denudation rates: A numerical modeling study of soil-mantled hillslopes. *Earth and Planetary Science Letters*, *272*(3–4), 591–599. https://doi.org/10.1016/j.epsl.2008.05.024

Ferrier, K. L., Kirchner, J. W., & Finkel, R. C. (2012). Weak influences of climate and mineral supply rates on chemical erosion rates: Measurements along two altitudinal transects in the Idaho Batholith. *Journal of Geophysical Research*, *117*(F2), F02026. https://doi.org/10.1029/2011jf002231

Ferrier, K. L., & Perron, J. T. (2020). The importance of hillslope scale in responses of chemical erosion rate to changes in tectonics and climate. *Journal of Geophysical Research: Earth Surface*, *125*(9), e2020JF005562. https://doi.org/10.1029/2020JF005562

Ferrier, K. L., Riebe, C. S., & Jesse Hahm, W. (2016). Testing for supply-limited and kinetic-limited chemical erosion in field measurements of regolith production and chemical depletion. *Geochemistry, Geophysics, Geosystems*, *17*(6), 2270–2285. https://doi.org/10.1002/2016gc006273

Ferrier, K. L., & West, N. (2017). Responses of chemical erosion rates to transient perturbations in physical erosion rates, and implications for relationships between chemical and physical erosion rates in regolith-mantled hillslopes. *Earth and Planetary Science Letters*, *474*, 447–456. https://doi.org/10.1016/j.epsl.2017.07.002

Fletcher, S. J. (2019). *Semi-Lagrangian advection methods and their applications in geoscience*. Elsevier. https://doi.org/10.1016/C2018-0-02183-0

Forte, A. M., Yanites, B. J., & Whipple, K. X. (2016). Complexities of landscape evolution during incision through layered stratigraphy with contrasts in rock strength. *Earth Surface Processes and Landforms*, *41*(12), 1736–1757. https://doi.org/10.1002/esp.3947

Fritsch, F. N., & Carlson, R. E. (1980). Monotone piecewise cubic interpolation. *SIAM Journal on Numerical Analysis*, *17*(2), 238–246. https://doi.org/10.1137/0717021

Gilbert, G. K. (1877). *Report on the Geology of the Henry Mountains*. US Government Printing Office.

Godard, V., Hippolyte, J. C., Cushing, E., Espurt, N., Fleury, J., Bellier, O., et al. (2020). Hillslope denudation and morphologic response to a rock uplift gradient. *Earth Surface Dynamics*, *8*(2), 221–243. https://doi.org/10.5194/esurf-8-221-2020

Granger, D. E., Kirchner, J. W., & Finkel, R. (1996). Spatially averaged long-term erosion rates measured from in situ-produced cosmogenic nuclides in alluvial sediment. *The Journal of Geology*, *104*(3), 249–257. https://doi.org/10.1086/629823

Grieve, S. W., Mudd, S. M., & Hurst, M. D. (2016). How long is a hillslope? *Earth Surface Processes and Landforms*, *41*(8), 1039–1054. https://doi.org/10.1002/esp.3884

Grischott, R., Kober, F., Lupker, M., Hippe, K., Ivy-Ochs, S., Hajdas, I., et al. (2017). Constant denudation rates in a high alpine catchment for the last 6 kyrs. *Earth Surface Processes and Landforms*, *42*(7), 1065–1077. https://doi.org/10.1002/esp.4070

Heimsath, A. M. (2006). Eroding the land: Steady-state and stochastic rates and processes through a cosmogenic lens. *Special Paper of the Geological Society of America*, *415*, 111–129. https://doi.org/10.1130/2006.2415(07)

Heimsath, A. M., Chappell, J., Spooner, N. A., & Questiaux, D. G. (2002). Creeping soil. *Geology*, *30*(2), 111–114. https://doi.org/10.1130/0091-7613(2002)030<0111:cs>2.0.co;2

Heimsath, A. M., Dietrich, W. E., Nishiizumi, K., & Finkel, R. C. (1997). The soil production function and landscape equilibrium. *Nature*, *388*(6640), 358–361. https://doi.org/10.1038/41056

Heimsath, A. M., Dietrich, W. E., Nishiizumi, K., & Finkel, R. C. (1999). Cosmogenic nuclides, topography, and the spatial variation of soil depth. *Geomorphology*, *27*(1–2), 151–172. https://doi.org/10.1016/S0169-555X(98)00095-6

Heimsath, A. M., Dietrich, W. E., Nishiizumi, K., & Finkel, R. C. (2001). Stochastic processes of soil production and transport: Erosion rates, topographic variation and cosmogenic nuclides in the Oregon Coast Range. *Earth Surface Processes and Landforms*, *26*(5), 531–552. https://doi.org/10.1002/esp.209

Hippe, K. (2017). Constraining processes of landscape change with combined in situ cosmogenic ^{14}C-^{10}Be analysis. *Quaternary Science Reviews*, *173*, 1–19. https://doi.org/10.1016/j.quascirev.2017.07.020

Hippe, K., Gordijn, T., Picotti, V., Hajdas, I., Jansen, J. D., Christl, M., et al. (2019). Fluvial dynamics and ^{14}C-^{10}Be disequilibrium on the Bolivian Altiplano. *Earth Surface Processes and Landforms*, *44*(3), 766–780. https://doi.org/10.1002/esp.4529

Hippe, K., Jansen, J. D., Skov, D. S., Lupker, M., Ivy-Ochs, S., Kober, F., et al. (2021). Cosmogenic in situ ^{14}C-^{10}Be reveals abrupt Late Holocene soil loss in the Andean Altiplano. *Nature Communications*, *12*(1), 1–9. https://doi.org/10.1038/s41467-021-22825-6

Hurst, M. D., Grieve, S. W., Clubb, F. J., & Mudd, S. M. (2019). Detection of channel-hillslope coupling along a tectonic gradient. *Earth and Planetary Science Letters*, *522*, 30–39. https://doi.org/10.1016/j.epsl.2019.06.018

Hurst, M. D., Mudd, S. M., Walcott, R., Attal, M., & Yoo, K. (2012). Using hilltop curvature to derive the spatial distribution of erosion rates. *Journal of Geophysical Research*, *117*(F2), F02017. https://doi.org/10.1029/2011jf002057

Kirchner, J. W., & Ferrier, K. L. (2013). Mainly in the plain. *Nature*, *495*(7441), 318–319. https://doi.org/10.1038/495318a

Knudsen, M. F., Egholm, D. L., & Jansen, J. D. (2019). Time-integrating cosmogenic nuclide inventories under the influence of variable erosion, exposure, and sediment mixing. *Quaternary Geochronology*, *51*, 110–119. https://doi.org/10.1016/j.quageo.2019.02.005

Lal, D. (1991). Cosmic ray labeling of erosion surfaces: In situ nuclide production rates and erosion models. *Earth and Planetary Science Letters*, *104*(2–4), 424–439. https://doi.org/10.1016/0012-821X(91)90220-C

Larsen, I. J., Almond, P. C., Eger, A., Stone, J. O., Montgomery, D. R., & Malcolm, B. (2014). Rapid soil production and weathering in the Southern Alps, New Zealand. *Science*, *343*(6171), 637–640. https://doi.org/10.1126/science.1244908

Lifton, N., Sato, T., & Dunai, T. J. (2014). Scaling in situ cosmogenic nuclide production rates using analytical approximations to atmospheric cosmic-ray fluxes. *Earth and Planetary Science Letters*, *386*, 149–160. https://doi.org/10.1016/j.epsl.2013.10.052

Lucas, T. R. (1974). Error bounds for interpolating cubic splines under various end conditions. *SIAM Journal on Numerical Analysis*, *11*(3), 569–584. https://doi.org/10.1137/0711049

Lucas, Y. (2001). The role of plants in controlling rates and products of weathering: Importance of biological pumping. *Annual Review of Earth and Planetary Sciences*, *29*(1), 135–163. https://doi.org/10.1146/annurev.earth.29.1.135

Marrero, S. M., Phillips, F. M., Borchers, B., Lifton, N., Aumer, R., & Balco, G. (2016). Cosmogenic nuclide systematics and the CRONUScalc program. *Quaternary Geochronology*, *31*, 160–187. https://doi.org/10.1016/j.quageo.2015.09.005

Marshall, J. A., Roering, J. J., Gavin, D. G., & Granger, D. E. (2017). Late Quaternary climatic controls on erosion rates and geomorphic processes in western Oregon, USA. *Bulletin*, *129*(5–6), 715–731. https://doi.org/10.1130/B31509.1

Mudd, S. M. (2017). Detection of transience in eroding landscapes. *Earth Surface Processes and Landforms*, *42*(1), 24–41. https://doi.org/10.1002/esp.3923

Mudd, S. M., & Furbish, D. J. (2007). Responses of soil-mantled hillslopes to transient channel incision rates. *Journal of Geophysical Research*, *112*(F3), F03S18. https://doi.org/10.1029/2006JF000516

Mudd, S. M., Harel, M. A., Hurst, M. D., Grieve, S. W., & Marrero, S. M. (2016). The CAIRN method: Automated, reproducible calculation of catchment-averaged denudation rates from cosmogenic nuclide concentrations. *Earth Surface Dynamics*, *4*(3), 655–674. https://doi.org/10.5194/esurf-4-655-2016

Neely, A. B., Bookhagen, B., & Burbank, D. W. (2017). An automated knickzone selection algorithm (KZ-Picker) to analyze transient landscapes: Calibration and validation. *Journal of Geophysical Research: Earth Surface*, *122*(6), 1236–1261. https://doi.org/10.1002/2017jf004250

Ott, R., Gallen, S. F., & Helman, D. (2023). Erosion and weathering in carbonate regions reveal climatic and tectonic drivers of carbonate landscape evolution. *Earth Surface Dynamics*, *11*(2), 247–257. https://doi.org/10.5194/esurf-11-247-2023

Ott, R. F., Gallen, S. F., & Granger, D. E. (2022). Cosmogenic nuclide weathering biases: Corrections and potential for denudation and weathering rate measurements. *Geochronology*, *4*(2), 455–470. https://doi.org/10.5194/gchron-4-455-2022

Pelletier, J. D. (2012). Fluvial and slope-wash erosion of soil-mantled landscapes: Detachment-or transport-limited? *Earth Surface Processes and Landforms*, *37*(1), 37–51. https://doi.org/10.1002/esp.2187

Perron, J. T. (2011). Numerical methods for nonlinear hillslope transport laws. *Journal of Geophysical Research*, *116*(F2). https://doi.org/10.1029/2010JF001801

Perron, J. T. (2017). Climate and the pace of erosional landscape evolution. *Annual Review of Earth and Planetary Sciences*, *45*(1), 561–591. https://doi.org/10.1146/annurev-earth-060614-105405

Perron, J. T., Dietrich, W. E., & Kirchner, J. W. (2008). Controls on the spacing of first-order valleys. *Journal of Geophysical Research*, *113*(F4), F04016. https://doi.org/10.1029/2007jf000977

Perron, J. T., Kirchner, J. W., & Dietrich, W. E. (2009). Formation of evenly spaced ridges and valleys. *Nature*, *460*(7254), 502–505. https://doi.org/10.1038/nature08174

Perron, J. T., Richardson, P. W., Ferrier, K. L., & Lapôtre, M. (2012). The root of branching river networks. *Nature*, *492*(7427), 100–103. https://doi.org/10.1038/nature11672

Portenga, E. W., & Bierman, P. R. (2011). Understanding Earth's eroding surface with ^{10}Be. *Geological Society of America Today*, *21*(8), 4–10. https://doi.org/10.1130/G111A.1

Reed, M. M., Ferrier, K. L., & Perron, J. T. (2023). CosmoTadpole 1.0 [Software]. Zenodo. https://doi.org/10.5281/zenodo.8256787

Richardson, P. W., Perron, J. T., Miller, S. R., & Kirchner, J. W. (2020). Modeling the formation of topographic asymmetry by aspect-dependent erosional processes and lateral channel migration. *Journal of Geophysical Research: Earth Surface*, *125*(7), e2019JF005377. https://doi.org/10.1029/2019JF005377

Richardson, P. W., Perron, J. T., & Schurr, N. D. (2019). Influences of climate and life on hillslope sediment transport. *Geology*, *47*(5), 423–426. https://doi.org/10.1130/G45305.1

Riebe, C. S., & Granger, D. E. (2013). Quantifying effects of deep and near-surface chemical erosion on cosmogenic nuclides in soils, saprolite, and sediment. *Earth Surface Processes and Landforms*, *38*(5), 523–533. https://doi.org/10.1002/esp.3339

Riebe, C. S., Kirchner, J. W., & Finkel, R. C. (2003). Long-term rates of chemical weathering and physical erosion from cosmogenic nuclides and geochemical mass balance. *Geochimica et Cosmochimica Acta*, *67*(22), 4411–4427. https://doi.org/10.1016/S0016-7037(03)00382-X

Riebe, C. S., Kirchner, J. W., & Finkel, R. C. (2004). Erosional and climatic effects on long-term chemical weathering rates in granitic landscapes spanning diverse climate regimes. *Earth and Planetary Science Letters*, *224*(3–4), 547–562. https://doi.org/10.1016/j.epsl.2004.05.019

Riebe, C. S., Kirchner, J. W., & Granger, D. E. (2001). Quantifying quartz enrichment and its consequences for cosmogenic measurements of erosion rates from alluvial sediment and regolith. *Geomorphology*, *40*(1–2), 15–19. https://doi.org/10.1016/s0169-555x(01)00031-9

Roering, J. J., Kirchner, J. W., & Dietrich, W. E. (1999). Evidence for nonlinear, diffusive sediment transport on hillslopes and implications for landscape morphology. *Water Resources Research*, *35*(3), 853–870. https://doi.org/10.1029/1998WR900090

Roering, J. J., Kirchner, J. W., & Dietrich, W. E. (2001). Hillslope evolution by nonlinear, slope-dependent transport: Steady state morphology and equilibrium adjustment timescales. *Journal of Geophysical Research*, *106*(B8), 16499–16513. https://doi.org/10.1029/2001JB000323

Schide, K., Gallen, S. F., & Lupker, M. (2022). Modelling the systematics of cosmogenic nuclide signals in fluvial sediments following extreme events. *Earth Surface Processes and Landforms*, *47*(9), 2325–2340. https://doi.org/10.1002/esp.5381

Skov, D. S., Egholm, D. L., Jansen, J. D., Sandiford, M., & Knudsen, M. F. (2019). Detecting landscape transience with in situ cosmogenic ^{14}C and ^{10}Be. *Quaternary Geochronology*, *54*, 101008. https://doi.org/10.1016/j.quageo.2019.101008

Small, E. E., Anderson, R. S., & Hancock, G. S. (1999). Estimates of the rate of regolith production using ^{10}Be and ^{26}Al from an alpine hillslope. *Geomorphology*, *27*(1–2), 131–150. https://doi.org/10.1016/S0169-555X(98)00094-4

Spiegelman, M., & Katz, R. F. (2006). A semi-Lagrangian Crank-Nicolson algorithm for the numerical solution of advection-diffusion problems. *Geochemistry, Geophysics, Geosystems*, *7*(4). https://doi.org/10.1029/2005gc001073

Sweeney, K. E., Roering, J. J., & Ellis, C. (2015). Experimental evidence for hillslope control of landscape scale. *Science*, *349*(6243), 51–53. https://doi.org/10.1126/science.aab0017

Theodoratos, N., & Kirchner, J. W. (2020). Dimensional analysis of a landscape evolution model with incision threshold. *Earth Surface Dynamics*, *8*(2), 505–526. https://doi.org/10.5194/esurf-8-505-2020

Torres, M. A., West, A. J., & Li, G. (2014). Sulphide oxidation and carbonate dissolution as a source of CO_2 over geological timescales. *Nature*, *507*(7492), 346–349. https://doi.org/10.1038/nature13030

von Blanckenburg, F. (2006). The control mechanisms of erosion and weathering at basin scale from cosmogenic nuclides in river sediment. *Earth and Planetary Science Letters*, *242*(3–4), 224–239. https://doi.org/10.1016/j.epsl.2005.11.017

Walker, J. C., Hays, P. B., & Kasting, J. F. (1981). A negative feedback mechanism for the long-term stabilization of Earth's surface temperature. *Journal of Geophysical Research*, *86*(C10), 9776–9782. https://doi.org/10.1029/jc086ic10p09776

West, A. J., Galy, A., & Bickle, M. (2005). Tectonic and climatic controls on silicate weathering. *Earth and Planetary Science Letters*, *235*(1–2), 211–228. https://doi.org/10.1016/j.epsl.2005.03.020

Willenbring, J. K., Codilean, A. T., & McElroy, B. (2013). Earth is (mostly) flat: Apportionment of the flux of continental sediment over millennial time scales. *Geology*, *41*(3), 343–346. https://doi.org/10.1130/g33918.1

Willett, S. D. (1999). Orogeny and orography: The effects of erosion on the structure of mountain belts. *Journal of Geophysical Research*, *104*(B12), 28957–28981. https://doi.org/10.1029/1999jb900248

Willett, S. D., McCoy, S. W., Perron, J. T., Goren, L., & Chen, C. Y. (2014). Dynamic reorganization of river basins. *Science*, *343*(6175), 1248765. https://doi.org/10.1126/science.1248765

Yanites, B. J., Tucker, G. E., & Anderson, R. S. (2009). Numerical and analytical models of cosmogenic radionuclide dynamics in landslide-dominated drainage basins. *Journal of Geophysical Research*, *114*(F1), F01007. https://doi.org/10.1029/2008JF001088

Yoo, K., Amundson, R., Heimsath, A. M., Dietrich, W. E., & Brimhall, G. H. (2007). Integration of geochemical mass balance with sediment transport to calculate rates of soil chemical weathering and transport on hillslopes. *Journal of Geophysical Research*, *112*(F2), F02013. https://doi.org/10.1029/2005JF000402

Zondervan, J. R., Stokes, M., Boulton, S. J., Telfer, M. W., & Mather, A. E. (2020). Rock strength and structural controls on fluvial erodibility: Implications for drainage divide mobility in a collisional mountain belt. *Earth and Planetary Science Letters*, *538*, 116221. https://doi.org/10.1016/j.epsl.2020.116221

References From the Supporting Information

Barnhart, K. R., Glade, R. C., Shobe, C. M., & Tucker, G. E. (2019). Terrainbento 1.0: A Python package for multi-model analysis in long-term drainage basin evolution. *Geoscientific Model Development*, *12*(4), 1267–1297. https://doi.org/10.5194/gmd-12-1267-2019

Chamberlain, C. P., Waldbauer, J. R., & Jacobson, A. D. (2005). Strontium, hydrothermal systems and steady-state chemical weathering in active mountain belts. *Earth and Planetary Science Letters*, *238*(3–4), 351–366. https://doi.org/10.1016/j.epsl.2005.08.005

Fagherazzi, S., Howard, A. D., & Wiberg, P. L. (2002). An implicit finite difference method for drainage basin evolution. *Water Resources Research*, *38*(7), 21−1–21−5. https://doi.org/10.1029/2001WR000721

Howard, A. D. (1994). A detachment-limited model of drainage basin evolution. *Water Resources Research*, *30*(7), 2261–2285. https://doi.org/10.1029/94wr00757

Lague, D. (2014). The stream power river incision model: Evidence, theory and beyond. *Earth Surface Processes and Landforms*, *39*(1), 38–61. https://doi.org/10.1002/esp.3462